



Comparative study of entropy distribution for generalized fluid between an inclined channel in the perspective of classical and non-Fourier's law



Nidhal Ben Khedher^{a,b}, Sohail Rehman^{c,*}, Sultan Alqahtani^d, Hashim^e, Sultan Alshehry^d

^a Department of Mechanical Engineering, College of Engineering, University of Ha'il, Ha'il 81451, Saudi Arabia

^b Laboratory of Thermal and Energetic Systems Studies (LESTE) at the National School of Engineering of Monastir, University of Monastir, Tunisia

^c Department of Mathematic, Islamia College, Peshawar, Pkistan

^d College of Engineering, Mechanical Engineering Department, King Khalid University, Abha, Saudi Arabia

^e Department of Mathematics & Statistics, The University of Haripur, Haripur 22620, Pakistan

ARTICLE INFO

Article history:

Received 28 October 2022

Revised 1 May 2023

Accepted 18 June 2023

Available online 12 July 2023

Keywords:

Generalized Carreau nanofluid
Modified Fick's and Fourier's laws
Entropy
Inclined channel
Variable thermal conductivity

ABSTRACT

The key challenge in the design of thermal appliances is to degrade entropy production with maximal energy dissipation to improve system efficiency in a variety of engineering applications, such as nozzle design, converging die, and rocket design. Due to the existence of both tangential and radial components, which have a significant impact on the fluid movement, coupled transport rates, and entropy development in an inclined channel presents a greater challenge. The current inquiry intended to address the combined impacts of Cattaneo-Christove (C-C) heat flux and classical theory on thermal dissipation, along with irreversibility distribution in a tilted porous media. The Carreau nanofluid confined between two finite intersecting plates in the presence of a porous Darcy-Forchheimer medium is examined. The C-C heat flux, variable thermal conductivity, and mass diffusivity are all used to investigate heat transport. The flow originates from a source located at the intersection of the plates and constitutes the momentum conservation. The investigation includes entropy and Bejan analysis. The premises guide the mathematical modelling of the flow field. Through bvp4c techniques, numerical solutions are attained. Converging section velocity increases in response to increased porosity and the Forchheimer number. Variation in temperature is significant when classical heat flux is reverted. Higher thermophoretic and porosity parameters result in a higher rate of entropy formation, while the Darcy parameter promotes drastic increase. Bejan is an escalating function of Brownian and Darcy parameters, while the porosity parameter causes it to fall. Porosity and the Forchheimer number regulate skin friction.

© 2023 Karabuk University. Publishing services by Elsevier B.V. This is an open access article under the CC BY-NC-ND license (<http://creativecommons.org/licenses/by-nc-nd/4.0/>).

1. Introduction

Recent advancement in air conditioning and refrigeration, medical treatments, metal spinning, the processing of food, nuclear reactor cooling, and damage to crops, crude oil and other industrial, biomedical, and engineering processes have increased interest in thermal and solute transport phenomena. Convective transport theories have been used to this point by various researchers studying heat and solvent transport mechanisms [1]. Considering the rapidity of wave transfer, this convective transport procedures concept is not applicable in all media. The mass and temperature relaxation times are included to help reduce this ineptitude. Cattaneo [2] initially refined the Fourier's law of heat conduction through the development of heat relaxation time,

leading to the movement of thermal energy in a realistic structure. When considering viscous dissipation, the Cattaneo-Christove heat flux model, which is modified with Cattaneo thermal relaxation and supplemented with the Oldroyd upper-convected model on the premise of Fourier's thermal conduction law. Models of heat and mass flux developed by Cattaneo and Christov describe the thermal and solutal properties of mass and heat movement. Numerous researchers have developed Fourier and Fick's laws in recent times to handle time relaxation in both concentration and temperature fields. Tibullo and Zampoli [3] stated the C-C conduction of heat model in an incompressible liquid. Straughan [4] considers C-C thermal analysis in convection viscous liquid. Haddad [5] communicated on the C-C thermal analysis for the porous surface Brinkman fluid model. Hayat et al. [6] highlight the C-C thermal and mass relaxation for magnetized flow using nanomaterial. Ali and Sandeep [7] researched the nonlinear radiation in Casson nanoliquid over a heated surface using C-C heat law. Entropy opti-

* Corresponding author.

E-mail address: srehman34@gatech.edu (S. Rehman).

Nomenclature

$u(r, \theta)$	Radial velocity (ms^{-1})	T_w, C_w	Temperature (K) and concentration (kgm^{-3}) at the walls
U_{max}	Maximum velocity (ms^{-1})	q, J_C	Heat (Wm^{-2}) and mass flux ($kgm^{-2}s^{-1}$)
(r, θ, z)	Polar coordinates	2α	Channel width
∇	Gradient operator	$S_{r\theta}$	Shear stress at the wall
$\frac{k_\infty}{(\rho c_p)_f}$	Thermal diffusivity (m^2/s)	β_1, β_2	Thermal and solutal relaxation time
k_∞	thermal conductivity at the free stream ($Wm^{-1}K^{-1}$)	ϵ_1, ϵ_2	Thermal conductivity variable and zero-mass flux variable
$(\rho c_p)_f$	heat capacitance of the fluid	$\tau_1 = \frac{(\rho c_p)_p}{(\rho c_p)_f}$	Ratio of heat capacitance
$(\rho c_p)_p$	heat capacitance of the nanoparticles	δ_E, δ_C	Non-Fourier model and Fickian's terms
τ	stress tensor	N_G'''	Local entropy ($Wm^{-3}K^{-1}$)
η	Dynamic viscosity ($kgm^{-1}s^{-1}$)	T_0, C_0	Average temperature and concentration between the wall and bulk
η_∞, η_0	Infinite and zero shear rate viscosity ($kgm^{-1}s^{-1}$)	\tilde{R}	Ideal gas constant ($8.31446261815324 J \cdot K^{-1} \cdot mol^{-1}$)
B_1	first kind Rivlin-Erickson tensor	ζ	Similarity variable
$\dot{\gamma}$	shear rate	$f(\zeta)$	Dimensionless velocity
ϵ	Material constant	$\Theta(\zeta)$	Dimensionless temperature
∇p	Pressure differential	$\Phi(\zeta)$	Dimensionless concentration
C_b	drag coefficient	C_f	Skin friction
K	porosity of the permeable medium	E_G	Total entropy rate
ϕ	porosity factor	Br	Brinkman number
n	Power index $1 < n < 2$	λ_1	Darcy number
D_B, D_T	Brownian and thermophoresis diffusion coefficients (m^2s^{-1})	λ_2	inertia parameter
ρ_f, ρ_p	Fluid and nanoparticles density (kg/m^3)	We	Weissenberg number
T, C	Fluid temperature (K) and concentration (kgm^{-3})	Re	Reynolds number
Pr	Prandtl number	N_b	Brownian diffusion parameter
N_t	Thermophoresis (diffusion)	Ec	Eckert number
χ	diffusion parameter	β_E, β_C	Thermal and solutal relaxation parameter
Be	Bejan number ($mol.m^{-3}$)		

mization in Casson nanoliquid radiating flow was elaborated by Waqas et al. [8] by taking C-C heat flux. The references [9] and [10] provide a selection of significant papers on C-C double diffusions.

Entropy production is an indicator of the disorder created when thermal energy is converted into mechanical work. Any isolated closed system has it as a fundamental characteristic. Entropy additionally addresses the properties of closed systems at the most minute scales and evaluates unpredictability at the molecular level. Rudolf Clausius first established the idea of entropy in 1850 by combining statistical and thermodynamic properties linked to isolated thermal systems. Entropy can be mathematically determined using the second law of thermodynamics. Bejan [11,12] provided irreversibility minimizing in the convective thermal flow concept. Mahesh et al. [13] covered entropy optimization in non-Fourier heat flux for hybrid nanomaterial flow towards a rotating disc with radiation impact in their study. Reddy et al. [14] investigated thermal transport assessment in magnetized nanofluid flow inside a square cage. Mondal and Mahapatra [15] have examined entropy reduction in convective nanomaterial flow with heat and solutal transfer in a trapezoidal cavity. Hayat et al. [16] discuss irreversibility studies in petrol oil and water based nanoliquid flow due to porosity wall. References [17,18,19,20] and [21] cover a few key points relating entropy.

The key characteristics of nanofluid is its ability to enhance heat conduction, which makes it one of the most significant qualities. The presence of the nanoparticles causes nanofluids to have greater thermal conductivity as compared to base fluids. Several factors have been identified as contributing to the improvement in thermal conductivity in nanofluids. The fact that nanoparticles have a large surface area and may transport heat more efficiently than bulk fluid is one of the key contributing aspects. The nanofluid entire thermal conductivity is influenced by the high thermal con-

ductivity of the nanoparticles themselves. The investigation of thermal conductivity, which is presumed to be constant, has drawn the attention of various authors. However, when fluid is exposed to temperature, its physical properties can alter significantly. The heat generated by internal friction and resulting rise in temperature has an impact on the fluid thermal conductivity for the fluids that are relevant to the theory of lubrication. Sorokin [22], covered the stability flow with linear temperature-dependent thermal conductivity. According to Sorokin findings, variations in temperature were brought on by relatively tiny changes in thermal conductivity. Pinarabsi [23] studied the temperature-dependent thermal conductivity of the fluid. According to Khan et al. [24], a non-Newtonian fluid with thermophysical characteristics and temperature-dependent viscosity was studied theoretically and mathematically over a heated infinite rotating disc. Thermal conductivity is the rate of heat transfer per temperature difference per unit area through a unit thickness of material. Sohail et al. [25] investigated radiative flow of nanofluid under variable thermal conductivity and diffusion using computational scheme. Naseem et al. [26] studied the occurrence of mass and heat transport with mutual influence of radiation, diffusion-thermo, thermal-diffusion, and fluctuating thermal conductivity over the porous surface together. On the mechanism of the effect of varying thermal conductivity Tarakanmu et al. [27] focused on three-dimensional nanofluid across a stretched surface. Ajibade and Umar [28] took into account how different thermal conductivity and viscosity affect the flow of mixed convection fluid and heat transmission through vertical channels. Some recent advancement relating the fluid flow and heat transfer with variable thermal conductivity are provided in the Refs. [29,30,31].

Flow through divergent and converging channel has many practical applications, including oil and gas, and underground water hydrology; the deformation of molten polymers using convergent

dies; cold doodling operations related to the production of polymers; and the preparation of goods in factories, hospitals, and automobiles and many others. The fluid flow across two inclined planes is a crucial and fundamental element of a physical model due to its significance in several fields, notably in mechanical, industrial, medical, and physiological activities. The flow of blood via capillaries and arteries, flows through canals, flows through cavities, and river flow are examples of converging/diverging channels. The Jeffery-Hamel flow is a class of flows that Jeffery [32] and Hamel [33] first identified in 1915 and 1916, respectively. These flows explain the outflow and inflow of a viscous, incompressible fluid in an intersecting channel with a particular angle 2α between the walls. Hence, when we consider flow from a source or sink in radial direction, we are thinking about a flow that behaves identically to itself and has no-slip boundary criteria at the walls. These constitutive equations have an accurate similarity solution in the specific case of two-dimensional flow over a channel with inclined plane walls intersecting at a vertex with a source or sink. The problem of the constant two-dimensional radial flow of a viscous fluid through non-parallel plane barriers was solved by Rosenhead [34] in 1940. A further remarkable example is the extensive investigation was conducted by Millsaps and Pohlhausen [35]. Apparently, flow through converging or diverging channels is significant to both Newtonian and non-Newtonian fluids. Over the past forty years, non-Newtonian fluid mechanics interactions between various fluid categories and structures (such as surfaces, channels, tubes, and wedges) have been studied. Tanner [36] discovered a correlation between apparent viscosity and the third rate of invariant deformed in the case of a viscoelastic non-Newtonian fluid inside conical walls. He also offered a model for low Reynolds numbers that describes the viscometric measurements of the behavior of an inelastic fluid in a cone. About two decades later, Moffatt et al. [37] discovered analytically, in the scenario of the two-dimensional flow of viscoelastic fluid between converging walls with varying viscosity, velocity discontinuity was rapidly expanding with the increase in the Reynolds number. For the converging/diverging incompressible viscoelastic fluid slow flow via cones and wedges [38], and flow of non-Newtonian fluid a few researchers [39,40,41] used analytical and numerical approaches to obtain approximate solutions from the following two decades.

The thermal transport with appropriate physical properties such coupled conduction, viscous dissipation, thermal radiations, chemical reaction, and variable thermal conductivity has a significant part in processing and managing the heat transfer in non-Newtonian fluid flow, which is crucial to highlight. Investigating non-Newtonian fluids in the existence of these physical phenomena is therefore thought to be a difficult problem for physicists, mathematicians, and engineers. For example, the power law fluid is acknowledged as an extensively used non-Newtonian fluid model in the context of shear thickening and thinning aspects, but other non-Newtonian fluid models, such as the second and third grade, and power-law fluid models, have shortcomings that prevent results from being best subject to flow relating towards physical happenings. Numerous industrially used materials, such as slurries, foams, emulsions, automobiles, power plant building, processing plastic foam, absorbing mining, bubbles, inkjet covering printing, and making mayonnaise, melting polymers, do not obey to Newton's law of viscosity. The shear thinning or pseudoplasticity of time-independent liquids, which is characterized by an apparent viscosity that declines with an increase in shear rate, is the characteristic of these fluids that are most frequently seen. One of the time-independent classes of non-Newtonian liquids is the Carreau fluid [42]. The appealing and widespread application of this fluid model, notably define the rheological performance of polymeric liquids and biological fluids. For instance, it is frequently used to design and predict the flow of polymeric liquids that

resemble biological fluids, such as blood, Xanthan gum, and polyacrylamide gel solutions. The Carreau prototype will be helpful for comparing the characteristics of Newtonian and non-Newtonian liquids in a limiting case. The effects of the velocity slip condition with thermal radiation for a time-dependent Carreau nanofluid flow across a stationary or moving wedge have been investigated by Khan et al. [43]. They made the argument that the moving wedge velocity profile stands out more than the static wedge. The three-dimensional flow of the Carreau nanofluid past a linearly stretched heated surface has been investigated by Hayat et al. [44]. In order to evaluate the impact of Cattaneo-Christov heat through MHD stagnation point stream of Carreau fluid through an extended and diminishing substrate of the cylinder, Khan et al. [45] adopted the shooting approach (bvp4c).

It is anticipated that subsequent investigations for channel problems are more challenging involving the flow of electrically conducting fluids would build on the existing research into the physics of flow across a horizontal convergent channel as the basis. The results could be useful for comprehending groundwater migration, filtration, and purification processes, as well as the passage of petroleum, natural gas, and groundwater through a storage tank in an oil or gas field. The conversion of kinetic and potential energy into thermal energy is demonstrated by the irreversible mechanisms of viscous dissipation, heat transfer, and mass transfer. The work done by a fluid on neighboring layers because of shear stresses is known, as viscous dissipation is involved. Inspired by the literature mentioned above, we present a comparative analysis on entropy optimization and heat transfer in the non-Newtonian fluid flow towards the convergent channel. The current study novelty concerns are as follows:

The application of Cattaneo-Christov energy and mass flux models to the flow of Carreau liquid through convergent channel.

To handle porosity effects with the Darcy Forchheimer, model a porous medium is considered at the channel boundaries.

The second rule of thermodynamics is used to compute the total entropy rate, which depends on four main irreversibilities, including heat transfer, fluid friction, mass transfer, and porosity.

In the context of heat and mass transfer investigation using the C-C theory, the simultaneous contribution of the dynamic thermal and mass relaxation time parameter as well as the non-linear dual phenomenon of the variable thermal conductivity and mass diffusion has not yet been examined.

Analysis of the difference between the fluid temperature for a flow field with and without a thermal realignment parameter. A brief comparison in the context of conventional and improved Fourier's law is presented to adjudge the thermal structure and heat loss mechanism.

2. Problem statement and mathematical formulation

We adopt steady, laminar, radial flow of an incompressible Carreau nanofluid for the investigation; along with non-Fourier's heat and non-Fick's mass flux models, as well as the impacts of entropy production and the no-slip condition (Fig. 1). At angle 2α , the channel walls are aligned. The walls are smooth with constant temperatures T_w and concentrations C_w . The nanofluid Buongiorno model is also used for the development of flow equations. The theory of C-C heat flux is used in the current analysis to calculate heat transfer instead of the classical Fourier's $q = -k(T)\nabla T$ and Fick's equation $J_C = -D_B\nabla C$. The cylinder-shaped polar coordinates (r, θ, z) are used for the mathematical modelling of the current inquiry. The

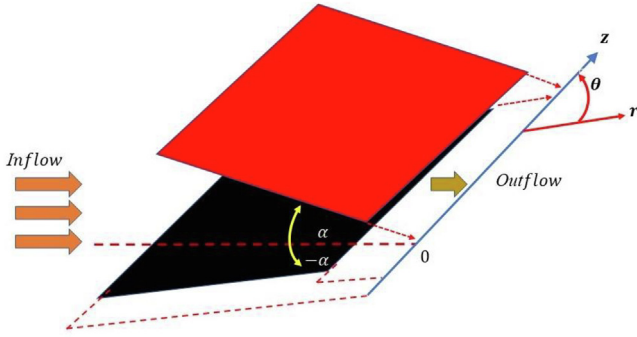


Fig. 1. Geometry of the flow with coordinates.

momentum equation utilizes the features of the Darcy-Forchhimer theory's formulation for non-Darcy porous media.

Using these premises, the boundary layer equations for thermal energy, mass, linear momentum, and nanoparticle volume friction are provided below in vector form [40].

$$\nabla \cdot (\rho_f V) = 0, \quad (1)$$

$$\rho_f (V \cdot \nabla) V = -\nabla p + \nabla \cdot \tau + F, \quad (2)$$

$$(\rho c_p)_f ((V \cdot \nabla) T) = -\nabla \cdot q + (\rho c_p)_p \left[D_B \nabla C \cdot \nabla T + \frac{D_T}{T_w} \nabla T \cdot \nabla T \right], \quad (3)$$

$$((V \cdot \nabla) C) = -\nabla \cdot J_C + \frac{D_T}{T_w} \nabla^2 T, \quad (4)$$

Here $V = u(r, \theta)$, $T = T(r, \theta)$, and $C = C(r, \theta)$, are flow field, temperature field and concentration. τ is the stress tensor, p is the pressure, $(D_B, D_T, \rho_f, \rho_p, c_p, q, J_C)$, are the Brownian and thermophoresis diffusion, fluid and nanoparticles density, energy, and concentration fluxes respectively.

2.1. Velocity distribution

The Cauchy stress tensor for Carreau fluid is defined as [46]

$$\tau = \eta B_1, \quad (5)$$

And

$$\frac{\eta - \eta_\infty}{\eta_0 - \eta_\infty} = \left[1 + (\dot{\gamma})^2 \right]^{0.5(n-1)}, \quad (6)$$

where η , is the fluid viscosity, η_∞ is the infinite-shear-rate viscosity, η_0 the zero-shear-rate viscosity, ϵ is a time material factor, n is the power-indexed, B_1 is the first kind Rivlin-Erickson tensor, and shear rate $\dot{\gamma}$ is defined as:

$$\dot{\gamma} = \sqrt{\frac{1}{2} \text{tr}(B_1)^2}, \quad (7)$$

In more practical situations $\eta_0 \gg \eta_\infty$, [47] thus $\eta_\infty = 0$, the equation reduces to

$$\eta = \eta_0 \left[1 + \epsilon^2 \left(2 \left(\frac{\partial u}{\partial r} \right)^2 + \frac{1}{r^2} \left(\frac{\partial u}{\partial \theta} \right)^2 + \frac{2u^2}{r^2} \right) \right]^{0.5(n-1)}, \quad (8)$$

The governing flow equation in r and θ components are [48,41]

$$\left(\frac{\partial}{\partial r} (\rho_f r u) \right) = 0, \quad (9)$$

$$\begin{aligned} u \frac{\partial u}{\partial r} = & -\frac{1}{\rho_f} \frac{\partial p}{\partial r} + v_f \left[\frac{\partial^2 u}{\partial r^2} + \frac{1}{r} \frac{\partial u}{\partial r} + \frac{1}{r^2} \frac{\partial^2 u}{\partial \theta^2} - \frac{u}{r^2} \right] \\ & \times \left[1 + \epsilon^2 \left\{ 2 \left(\frac{\partial u}{\partial r} \right)^2 + \frac{1}{r^2} \left(\frac{\partial u}{\partial \theta} \right)^2 + \frac{2u^2}{r^2} \right\} \right]^{0.5(n-1)} \\ & + v_f \epsilon^2 (n-1) \left[1 + \epsilon^2 \left\{ 2 \left(\frac{\partial u}{\partial r} \right)^2 + \frac{1}{r^2} \left(\frac{\partial u}{\partial \theta} \right)^2 + \frac{2u^2}{r^2} \right\} \right]^{0.5(n-3)} \\ & \times \left[4 \left(\frac{\partial u}{\partial r} \right)^2 \frac{\partial^2 u}{\partial r^2} + \frac{6}{r^2} \left(\frac{\partial u}{\partial r} \right) \left(\frac{\partial u}{\partial \theta} \right) \left(\frac{\partial^2 u}{\partial r \partial \theta} \right) - \frac{2}{r^2} \left(\frac{\partial u}{\partial r} \right) \left(\frac{\partial u}{\partial \theta} \right)^2 \right. \\ & \left. + \frac{4u}{r^2} \left(\frac{\partial u}{\partial r} \right)^2 - \frac{4u^2}{r^3} \frac{\partial u}{\partial r} + \frac{2}{r^4} \left(\frac{\partial u}{\partial \theta} \right)^2 \frac{\partial^2 u}{\partial \theta^2} + \frac{4u}{r^4} \left(\frac{\partial u}{\partial \theta} \right)^2 \right] \\ & - v_f \frac{\phi}{K} u - \frac{C_b \phi}{\sqrt{K}} u^2, \end{aligned}$$

$$\begin{aligned} 0 = & -\frac{1}{\rho_f r} \frac{\partial p}{\partial \theta} + \frac{2v_f}{r^2} \left[1 + \epsilon^2 \left\{ 2 \left(\frac{\partial u}{\partial r} \right)^2 + \frac{1}{r^2} \left(\frac{\partial u}{\partial \theta} \right)^2 + \frac{2u^2}{r^2} \right\} \right]^{0.5(n-1)} \frac{\partial u}{\partial \theta} \\ & + v_f \epsilon^2 \frac{(n-1)}{2r} \left[1 + \epsilon^2 \left\{ 2 \left(\frac{\partial u}{\partial r} \right)^2 + \frac{1}{r^2} \left(\frac{\partial u}{\partial \theta} \right)^2 + \frac{2u^2}{r^2} \right\} \right]^{0.5(n-3)} \\ & \times \left[4 \left(\frac{\partial u}{\partial r} \right) \left(\frac{\partial u}{\partial \theta} \right) \left(\frac{\partial^2 u}{\partial r^2} \right) + \frac{2}{r^2} \left(\frac{\partial u}{\partial \theta} \right)^2 \left(\frac{\partial^2 u}{\partial r \partial \theta} \right) - \frac{2}{r^3} \left(\frac{\partial u}{\partial \theta} \right)^3 \right. \\ & \left. + \frac{4u}{r^2} \left(\frac{\partial u}{\partial \theta} \right) \left(\frac{\partial u}{\partial r} \right) - \frac{4u}{r^3} \left(\frac{\partial u}{\partial \theta} \right) + 8u \left(\frac{\partial u}{\partial r} \right) \left(\frac{\partial^2 u}{\partial r \partial \theta} \right) \right. \\ & \left. + \frac{4u}{r^2} \left(\frac{\partial u}{\partial \theta} \right) \left(\frac{\partial^2 u}{\partial \theta^2} \right) + \frac{8u^2}{r^2} \frac{\partial u}{\partial \theta} \right] \end{aligned} \quad (11)$$

With the following boundary conditions [49,39]

$$\left[\begin{aligned} u &= U_{\max}, \quad \frac{\partial u}{\partial \theta} = 0, \quad \text{at } \theta = 0, \\ u &= 0, \quad \text{at } \theta = \pm \alpha \end{aligned} \right], \quad (12)$$

Here, $C_b = \frac{C_b^*}{r}$ indicate the drag coefficient, K is the permeability of the porous medium and ϕ is the porosity factor.

The coefficient of skin friction C_f can be defined as

$$C_f = \frac{S_{r\theta}}{\rho_f U_{\max}^2}, \quad (13)$$

Where the shear stress $S_{r\theta}$ at the wall surface is given below

$$S_{r\theta} = \eta_0 \left[1 + \epsilon^2 \left\{ 2 \left(\frac{\partial u}{\partial r} \right)^2 + \frac{1}{r^2} \left(\frac{\partial u}{\partial \theta} \right)^2 + \frac{2u^2}{r^2} \right\} \right]^{0.5(n-1)} \frac{1}{r} \left(\frac{\partial u}{\partial \theta} \right) \Big|_{\theta=\alpha}, \quad (14)$$

$$C_f = \frac{\eta_0}{\rho_f U_{\max}^2} \left[1 + \epsilon^2 \left\{ 2 \left(\frac{\partial u}{\partial r} \right)^2 + \frac{1}{r^2} \left(\frac{\partial u}{\partial \theta} \right)^2 + \frac{2u^2}{r^2} \right\} \right]^{\frac{n-1}{2}} \frac{1}{r} \left(\frac{\partial u}{\partial \theta} \right) \Big|_{\theta=\alpha}. \quad (15)$$

2.2. Thermal equation

The temperature equation in the view of C-C heat flux theory, by assuming steady state i.e., $\frac{\partial q}{\partial t} = 0$, and $(\nabla \cdot V) = 0$ for (incompressible flow). The corresponding heat flux $q = -k(T) \nabla T$ satisfy the non-Fourier's theory [50]

$$q + \beta_1 (V \cdot \nabla q - q \cdot \nabla V) = -k(T) \nabla T, \quad (16)$$

Where β_1 the thermal relaxation time and $K(T)$ is the temperature dependent thermal conductivity [51,52]:

$$k(T) = k_\infty [1 + \epsilon_1 \Theta(\zeta)]. \quad (17)$$

Where k_∞ is the thermal conductivity at the free stream, ϵ_1 is the thermal conductivity variable. The classical Fourier's law reverts on setting $\beta_1 = 0$. Thus, energy equation in the present scenario is

$$u \frac{\partial T}{\partial r} = -\nabla \cdot q + \tau_1 \left(D_B \left[\frac{\partial T}{\partial r} \frac{\partial C}{\partial r} + \frac{1}{r^2} \frac{\partial T}{\partial \theta} \frac{\partial C}{\partial \theta} \right] + \frac{D_T}{T_w} \left[\left(\frac{\partial T}{\partial r} \right)^2 + \frac{1}{r^2} \left(\frac{\partial T}{\partial \theta} \right)^2 \right] \right), \quad (18)$$

$$\begin{aligned} u \frac{\partial T}{\partial r} + \beta_1 \delta_E = & \frac{k_\infty}{(\rho c_p)_f} [1 + \epsilon_1 \Theta(\zeta)] \left[\frac{1}{r} \frac{\partial T}{\partial r} + \frac{\partial^2 T}{\partial r^2} + \frac{1}{r^2} \frac{\partial^2 T}{\partial \theta^2} \right] \\ & + \frac{k_\infty \epsilon_1}{(\rho c_p)_f} \left(\frac{1}{r} \frac{\partial T}{\partial r} \Theta(\zeta) + \frac{1}{\alpha r^2} \frac{\partial T}{\partial \theta} \Theta'(\zeta) \right) \\ & + \tau_1 \left(D_B \left[\frac{\partial T}{\partial r} \frac{\partial C}{\partial r} + \frac{1}{r^2} \frac{\partial T}{\partial \theta} \frac{\partial C}{\partial \theta} \right] + \frac{D_T}{T_w} \left[\left(\frac{\partial T}{\partial r} \right)^2 + \frac{1}{r^2} \left(\frac{\partial T}{\partial \theta} \right)^2 \right] \right), \end{aligned} \quad (19)$$

where

$$\begin{aligned} \delta_E = & \left[u \frac{\partial u}{\partial r} \frac{\partial T}{\partial r} + u^2 \frac{\partial^2 T}{\partial r^2} \right] + 2 \left[1 + \epsilon^2 \left\{ 2 \left(\frac{\partial u}{\partial r} \right)^2 + \frac{1}{r^2} \left(\frac{\partial u}{\partial \theta} \right)^2 + \frac{2u^2}{r^2} \right\} \right]^{0.5(n-1)} \\ & \times \left[2u \left(\frac{\partial u}{\partial r} \right) \frac{\partial^2 u}{\partial r^2} - \frac{2u}{r^3} \left(\frac{\partial u}{\partial \theta} \right)^2 + \frac{u}{r^2} \frac{\partial^2 u}{\partial r \partial \theta} \frac{\partial u}{\partial \theta} + \frac{2u^2}{r^2} \left(\frac{\partial u}{\partial \theta} \right) - \frac{2u^3}{r^3} \right] \\ & - \tau_1 D_B \left[u \frac{\partial^2 C}{\partial r^2} \frac{\partial T}{\partial r} + u \frac{\partial^2 T}{\partial r^2} \frac{\partial C}{\partial r} - \frac{2u^2}{r^3} \frac{\partial T}{\partial \theta} \frac{\partial C}{\partial \theta} \right. \\ & \left. + u \frac{\partial^2 T}{\partial r \partial \theta} \frac{\partial C}{\partial \theta} + \frac{u}{r^2} \frac{\partial^2 C}{\partial r \partial \theta} \frac{\partial T}{\partial \theta} \right] \\ & - 2 \frac{\tau_1 D_T}{T_w} \left[u \frac{\partial u}{\partial r} \frac{\partial^2 T}{\partial r^2} - \frac{u}{r^3} \left(\frac{\partial T}{\partial \theta} \right)^2 + \frac{u}{r^2} \frac{\partial u}{\partial \theta} \frac{\partial^2 T}{\partial r \partial \theta} \right], \end{aligned} \quad (20)$$

In above expression $\tau_1 = \frac{(\rho c_p)_p}{(\rho c_p)_f}$, is the thermal capacity ratio.

With the subsequent boundary conditions:

$$\left. \begin{aligned} \frac{\partial T}{\partial \theta} &= 0, & \text{at } \theta &= 0 \\ T &= T_w, & \text{at } \theta &= \pm \alpha \end{aligned} \right\}, \quad (21)$$

2.3. Nanoparticles volume friction

The mass flux according to C-C heat flux theory can be express as [51]

$$J_C + \beta_2 (V \cdot \nabla J_C - J_C \cdot \nabla V) = -D_B(C) \nabla C, \quad (22)$$

Where β_2 is the concentration time relaxation time, J_C is the mass flux. Here, $D_B(C)$ is the concentration dependent mass diffusivity is defined as:

$$D_B(C) = D_B [1 + \epsilon_2 \Phi(\zeta)] \quad (23)$$

$$u \frac{\partial C}{\partial r} = -\nabla \cdot J_C + \frac{D_T}{T_w} \left[\frac{1}{r} \frac{\partial T}{\partial r} + \frac{\partial^2 T}{\partial r^2} + \frac{1}{r^2} \frac{\partial^2 T}{\partial \theta^2} \right], \quad (24)$$

$$\begin{aligned} u \frac{\partial C}{\partial r} + \beta_2 \delta_C = & D_B \epsilon_2 \left(\frac{1}{r} \frac{\partial C}{\partial r} \Phi(\zeta) + \frac{1}{\alpha r^2} \frac{\partial C}{\partial \theta} \Phi'(\zeta) \right) \\ & + D_B [1 + \epsilon_2 \Phi(\zeta)] \left(\frac{1}{r} \frac{\partial C}{\partial r} + \frac{\partial^2 C}{\partial r^2} + \frac{1}{r^2} \frac{\partial^2 C}{\partial \theta^2} \right) \\ & + \frac{D_T}{T_w} \left[\frac{1}{r} \frac{\partial T}{\partial r} + \frac{\partial^2 T}{\partial r^2} + \frac{1}{r^2} \frac{\partial^2 T}{\partial \theta^2} \right], \end{aligned} \quad (25)$$

$$\begin{aligned} \delta_C = & \left[u \frac{\partial u}{\partial r} \frac{\partial C}{\partial r} + u^2 \frac{\partial^2 C}{\partial r^2} \right] \\ & - \frac{D_T}{T_w} \left[u \frac{\partial^3 T}{\partial r^3} - \frac{u}{r^2} \frac{\partial T}{\partial r} + u \frac{\partial^2 T}{\partial r^2} - \frac{2u^2}{r^3} \frac{\partial^2 T}{\partial \theta^2} + \frac{u}{r^2} \frac{\partial^3 T}{\partial r \partial \theta^2} \right], \end{aligned} \quad (26)$$

with geometrical boundary conditions

$$\left. \begin{aligned} \frac{\partial C}{\partial \theta} &= 0, & \text{at } \theta &= 0, \\ C &= C_w, & \text{at } \theta &= \pm \alpha \end{aligned} \right\}. \quad (27)$$

2.4. Entropy production features

Entropy production equation for the Carreau nanoliquid across an inclined channel occurs as a consequence of energy loss [53,54,55].

$$\begin{aligned} N_G''' = & \frac{K_f}{T_0^2} [\nabla T \cdot \nabla T] + \frac{1}{T_0} [\tau \cdot L] + \frac{\eta_f}{T_0 K} u^2 + \frac{\rho_f C_b}{\sqrt{K T_0}} u^2 \\ & + \frac{\tilde{R} D_B}{T_0} [\nabla T \cdot \nabla C] + \frac{\tilde{R} D_B}{C_0} [\nabla C \cdot \nabla C], \end{aligned} \quad (28)$$

Four terms are employed to define entropy generation in this context. These terms, which refer to the irreversibility of heat transport, fluid friction, porous medium and concentration, respectively, imply the production of entropy. Entropy production expression is:

$$\begin{aligned} N_G''' = & \underbrace{\frac{K_f}{T_0^2} \left[\left(\frac{\partial T}{\partial r} \right)^2 + \frac{1}{r^2} \left(\frac{\partial T}{\partial \theta} \right)^2 \right]}_{\text{Heat transfer irreversibility}} \\ & + \underbrace{\frac{\eta_f}{T_0} \left(1 + \epsilon^2 \left\{ 2 \left(\frac{\partial u}{\partial r} \right)^2 + \frac{1}{r^2} \left(\frac{\partial u}{\partial \theta} \right)^2 + \frac{2u^2}{r^2} \right\} \right)}_{\text{Viscous dissipation irreversibility}} \underbrace{\left(1 + \epsilon^2 \left\{ 2 \left(\frac{\partial u}{\partial r} \right)^2 + \frac{1}{r^2} \left(\frac{\partial u}{\partial \theta} \right)^2 + \frac{2u^2}{r^2} \right\} \right)}_{\text{Porous matrix}} \\ & + \underbrace{\frac{\eta_f}{T_0 K} u^2 + \frac{\rho_f C_b}{T_0 \sqrt{K}} u^2}_{\text{porous matrix}} + \underbrace{\frac{\tilde{R} D_B}{C_0} \left[\left(\frac{\partial C}{\partial r} \right)^2 + \frac{1}{r^2} \left(\frac{\partial C}{\partial \theta} \right)^2 \right] + \frac{\tilde{R} D_B}{T_0} \left[\frac{\partial T}{\partial r} \frac{\partial C}{\partial r} + \frac{1}{r^2} \frac{\partial T}{\partial \theta} \frac{\partial C}{\partial \theta} \right]}_{\text{Mass transfer irreversibility}}. \end{aligned} \quad (29)$$

where

$$T_0 = \frac{T + T_w}{2}, C_0 = \frac{C + C_w}{2}. \quad (30)$$

In the above equation N_G''' designates the local volumetric entropy production rate and its ratio with the characteristic rate of entropy generation N_G''' is familiar as the entropy generation number and T_0 and C_0 are the average temperature and concentration.

2.5. The explication for the problem

The preceding flow equations are transmuted by incorporating the following similarity quantities that transform the established nonlinear PDEs into the system of ODEs. By invoking the following similarity transformation [56,57,58]

$$f(\zeta) = \frac{g(\theta)}{r U_{\max}}, \zeta = \frac{\theta}{\alpha}, \Theta(\zeta) = \frac{T}{T_w}, \Phi(\zeta) = \frac{C}{C_w}. \quad (31)$$

where $g(\theta)$ in the view of continuity equation gives

$$g(\theta) = ru(r, \theta). \quad (32)$$

The similarity transformation stated in Eq. (31), when applied, to the governing PDE stated in Eqs. and (10), (11), (19), (25) and (29) with associated constraints at the channel walls and at the central portion of the channel, the following ODEs, each of which depends only on the single independent variable ζ as follows:

Dimensionless form of momentum equation

$$\begin{aligned}
& \left[\frac{d^3 f}{d\zeta^3} + 4\alpha^2 \frac{df}{d\zeta} \right] \left[1 + We^2 \left\{ \left(\frac{df}{d\zeta} \right)^2 + 4\alpha^2 f^2 \right\} \right]^{0.5(n-1)} + 2\alpha Re_f \left(\frac{df}{d\zeta} \right) \\
& - \lambda_1 \alpha Re \left(\frac{df}{d\zeta} \right) - 2\lambda_2 \alpha Re_f \left(\frac{df}{d\zeta} \right) \\
& + (n-1) We^2 \left[1 + We^2 \left\{ \left(\frac{df}{d\zeta} \right)^2 + 4\alpha^2 f^2 \right\} \right]^{0.5(n-3)} \\
& \times \left(3 \left(\frac{df}{d\zeta} \right) \left(\frac{d^2 f}{d\zeta^2} \right)^2 + 32\alpha^2 f \left(\frac{df}{d\zeta} \right) \left(\frac{d^2 f}{d\zeta^2} \right) + \left(\frac{df}{d\zeta} \right)^2 \left(\frac{d^3 f}{d\zeta^3} \right) + 64\alpha^4 \frac{df}{d\zeta} f^2 \right) \\
& + (n-1)(n-3) \left(We^2 \right)^2 \left[1 + We^2 \left\{ \left(\frac{df}{d\zeta} \right)^2 + 4\alpha^2 f^2 \right\} \right]^{0.5(n-5)} \\
& \left(\left(\frac{df}{d\zeta} \right)^3 \left(\frac{d^2 f}{d\zeta^2} \right)^2 + 16\alpha^2 f \left(\frac{df}{d\zeta} \right)^3 \left(\frac{d^2 f}{d\zeta^2} \right) + 32\alpha^4 \left(\frac{df}{d\zeta} \right) \left(\frac{d^2 f}{d\zeta^2} \right) \right. \\
& \left. + 16\alpha^4 f^2 \left(\frac{df}{d\zeta} \right)^3 + 64\alpha^6 f^4 \left(\frac{df}{d\zeta} \right) - 4\alpha^2 \left(\frac{df}{d\zeta} \right)^5 \right) = 0,
\end{aligned} \tag{33}$$

With the dimensionless boundary conditions

$$f(0) = 1, \frac{df(0)}{d\zeta} = 0 = 0, f(\pm 1) = 0. \tag{34}$$

$$\Phi(\pm 1) = 1, \frac{d\Phi(0)}{d\zeta} = 0. \tag{38}$$

Dimensionless physical quantities

$$C_f = \frac{1}{Re} \left[\left(1 + We^2 \left(4\alpha^2 f^2(1) + f'^2(1) \right) \right)^{\frac{n-1}{2}} f'(1) \right], \tag{39}$$

Dimensionless form of entropy generation

$$E_G = \frac{r^2 \alpha^2 N_G'''}{\kappa_f}, \tag{40}$$

$$\begin{aligned}
E_G &= \left(\frac{d\Theta}{d\zeta} \right)^2 \\
&+ Br \left[\left(1 + We^2 \left\{ \left(\frac{df}{d\zeta} \right)^2 + 4\alpha^2 f^2 \right\} \right)^{0.5(n-1)} \right] \left(\left(\frac{df}{d\zeta} \right)^2 + 4\alpha^2 f^2 \right) \\
&+ Br \lambda_1 f^2 + Br \lambda_2 \left(\frac{df}{d\zeta} \right)^2 + \chi \left(\left(\frac{d\Phi}{d\zeta} \right)^2 + \left(\frac{d\Phi}{d\zeta} \right) \left(\frac{d\Theta}{d\zeta} \right) \right),
\end{aligned} \tag{41}$$

Bejan number (*Be*), commonly referred to as the entropy fabrication ratio caused by heat transport irreversibility to the overall entropy production.

$$Be = \frac{\left(\frac{d\Theta}{d\zeta} \right)^2}{\left(\frac{d\Theta}{d\zeta} \right)^2 + Br \left[\left(1 + We^2 \left\{ \left(\frac{df}{d\zeta} \right)^2 + 4\alpha^2 f^2 \right\} \right)^{0.5(n-1)} \right] \left(\left(\frac{df}{d\zeta} \right)^2 + 4\alpha^2 f^2 \right) + Br \lambda_1 f^2 + Br \lambda_2 \left(\frac{df}{d\zeta} \right)^2 + \left(\left(\frac{d\Phi}{d\zeta} \right)^2 \chi + \left(\frac{d\Phi}{d\zeta} \right) \left(\frac{d\Theta}{d\zeta} \right) \right)}, \tag{42}$$

Dimensionless form of energy equation

$$\begin{aligned}
& \frac{d^2 \Theta}{d\zeta^2} + \epsilon_1 \Theta \frac{d^2 \Theta}{d\zeta^2} + \epsilon_1 \left(\frac{d\Theta}{d\zeta} \right)^2 + \left(Pr N_b \frac{d\Theta}{d\zeta} \frac{d\Phi}{d\zeta} + Pr N_t \left(\frac{d\Theta}{d\zeta} \right)^2 \right) \\
& + Pr Ec \left[1 + We^2 \left\{ \left(\frac{df}{d\zeta} \right)^2 + 4\alpha^2 f^2 \right\} \right]^{0.5(n-1)} \left\{ \left(\frac{df}{d\zeta} \right)^2 + 4\alpha^2 f^2 \right\} \\
& - 2\beta_E Pr Ec \left[1 + We^2 \left\{ \left(\frac{df}{d\zeta} \right)^2 + 4\alpha^2 f^2 \right\} \right]^{0.5(n-1)} \\
& \times \left(3 \left(\frac{d\Theta}{d\zeta} \right)^2 \Theta + 8\alpha^2 \left(\frac{d\Theta}{d\zeta} \right)^3 \right) \\
& - 2\beta_E \left(Pr N_b \frac{d\Theta}{d\zeta} \frac{d\Phi}{d\zeta} + Pr N_t \left(\frac{d\Theta}{d\zeta} \right)^2 \right) = 0,
\end{aligned} \tag{35}$$

Associated dimensionless boundary conditions are:

$$\Theta(\pm 1) = 1, \frac{d\Theta(0)}{d\zeta} = 0, \tag{36}$$

Dimensionless form of concentration equation

$$\frac{d^2 \Phi}{d\zeta^2} + \epsilon_2 \Phi \frac{d^2 \Phi}{d\zeta^2} + \epsilon_2 \left(\frac{d\Phi}{d\zeta} \right)^2 + \frac{N_t}{N_b} \left(\frac{d^2 \Theta}{d\zeta^2} \right) - 2\beta_c \frac{N_t}{N_b} \left(\frac{d\Theta}{d\zeta} \right) \left(\frac{d^2 \Theta}{d\zeta^2} \right) = 0, \tag{37}$$

With

Here,

$$\begin{aligned}
\lambda_1 &= \frac{\nu_f \phi}{K U_{max}} : \lambda_2 = \frac{C_b \phi}{\sqrt{K}} : We = \left(\frac{\sqrt{\epsilon^2 U_{max}^2}}{r^2 \alpha^2} \right) : Re = \left(\frac{\alpha r U_{max}}{\nu_f} \right) : \\
Pr &= \left(\frac{\mu C_p}{k_f} \right) : Br = Pr Ec : \chi = \left(\frac{\tilde{R} D_B C_w}{\kappa_f} \right) : \\
N_b &= \left(\frac{\tau D_B C_w}{\nu_f} \right) : N_t = \left(\frac{\tau D_T T_w}{\nu_f T_\infty} \right) : Ec = \left(\frac{U_{max}^2}{T_w C_p} \right) : \beta_E (= \epsilon_E u) : \beta_C (= \epsilon_C u) : \epsilon_1 : \epsilon_2 :
\end{aligned}$$

Is the Darcy number, inertia parameter, Weissenberg: Reynolds number: Prandtl: The Brinkman: The diffusion parameter: The Brownian parameter: Thermophoresis (diffusion): The Eckert: Thermal and solutal relaxation parameter: \tilde{R} is the molar gas constant, signifies minor parameters known as variable thermal conductivity and zero-mass flux parameters.

3. Solution scheme

It is almost impossible to conceive the closed-form solutions to the governing normalized equations (33), (35), (37) and (41) because of highly non-linear nature. Therefore, a numerical treatment to the model problem is made for the sake of solutions. The system of normalized equations (33), (35), and (37) are switched to the initial value. The built-in routine of MATLAB, bvp4c [59] is employed for numerical simulation. Setting $\zeta = 1$, with an accuracy of 10^{-5} for the outer boundary conditions yields the solutions. Two estimations are developed and correlated at each step after the appropriate step size $\zeta = 0.01$ has been determined. If

these two projections are reasonably in accord with one another, it is acceptable. Otherwise, until the required accuracy is attained, the step size once again is reduced, and the calculation is performed. The selection of acceptable finite values for the similarity variable is the most important component of this technique. An initial guess is made for a specific set of physical variables to achieve the velocity $f(0)$, temperature $\Theta(0)$ and concentration $\Phi(0)$ fields to evaluate for the specific boundary value problem given by Eqs. (34), (36) and (38). Until three consecutive values of $f(0)$, $\Theta(0)$ and $\Phi(0)$ differ only by the identified significant figures, the method is repeated with a higher value of ζ . The ultimate value of ζ is chosen to be the limit best-suited value for that set of variables. For a different set of parameters, the value of ζ may differ. The coupled boundary value issue is solved numerically using the superposition method for the specified term of. The accuracy of up to four decimal places and the step size of $\zeta = 0.001$ are chosen as the computation convergence requirements. The values of missing conditions chosen here are (1, 1, 0, 0, 0, 0, 0), then the problem is tickled by bvp4c methodology.

3.1. Validations of the model

The comparative numerical solutions (bvp4c solutions) for convergent and divergent channels are illustrated in Tables 1 and Table 2, respectively. These tables reveal that for $\zeta = 0$, to $\zeta = 1$ the obtained solutions are in perfect alignment with published literature.

4. Dimensionless analysis

In the current study, we have numerically analyzed the possible arrangements of parameter paired on the channel boundaries of an inclined porous annular enclosure for the converging channel flow of Carreau liquid and associated heat transport as well as entropy production. The effects of different parameters are investigated, including geometric inclination angle, porosity parameter, and Darcy number. Entropy generation contours and curves are used to demonstrate the flow pattern, thermal fields, and irreversibility distribution. Velocity distribution is analyzed in convergent and divergent sections. The thermal, concentration, entropy and Bejan profile are plotted and analyzed. Each effect is securitized in the scenario of thermal relaxation involvement $\beta_E (= 0.2)$ and classical heat flux model $\beta_E (= 0.0)$.

4.1. Velocity distribution of Carreau liquid

The structural characteristics of the emerging Carreau nanofluid in convergent/divergent flow are illustrated graphically in this section. The solid lines indicate convergent flow $\alpha < 0$ behavior for fixed inclination angles of $\alpha = -10^\circ$, while the second figure represent divergent flow $\alpha > 0$ behaviour in the plots shown here. In Fig. 2, the fluctuation of the velocity field vs the porosity parameter λ_1 is displayed for both convergent and divergent situations. The curves shows that the velocity field increases for increasing values of λ_1 , when $\alpha = -10^\circ$ and decreases for $\alpha = 10^\circ$. Here, it is seen

that the substantial resistive effects are responsible for the reducing the velocity in the divergent case because they slow down the fluid rate of deformation of the material. Additionally, it can be observed in the convergent case that momentum thickness increases as λ_1 increases, suggesting that the growth is related to a sustaining of the permeability effects, which results in a significant increase in momentum thickness. Furthermore, strong permeability accelerates velocity because it enhances the rate of fluid deformation in the flow. Physical inertia parameter λ_2 v/s velocity fluctuations $f(\zeta)$ in converging and diverging channels are seen in Fig. 3. It demonstrates that in a converging channel, the velocity field increases as the inertia parameter rises, whereas in a diverging channel, the flow description is the opposite. Physically, as the λ_2 increases, the surface drag increases and reduces pore velocity, which causes the velocity in the diverging channel to decrease. Additionally, it is evident that increasing values of λ_2 cause the flow rate to increase and the fluid to deform more quickly. It makes sense that non-Darcy phenomena would contribute to the improvement of permeability effects. As a result, increased permeability effects increase the rate of deformation, which aids in amplifying the flow velocity in a converging channel. In essence, the nonlinear inertia term increases the fluid flow nonlinearity, which results in a sharp peak in velocity close to the surface channel.

4.2. Fluid temperature analysis

Fig. 4 investigates the variations in the fluid temperature profiles for various Prandtl number values. Because temperature profiles in the boundary region rapidly decrease for large values of Pr , this plot shows that the liquid temperature declines as Prandtl number increases. In addition, when the Prandtl number values increase, the boundary layer thickness decreases. For the fluid, it creates a connection between momentum and thermal diffusivities. As a result, the amount of heat from the fluid diffuses more quickly than momentum diffusivity due to lower Pr values. As a result, the thermal border region observes notable fluctuations in the temperature gradient profiles. Thermal diffusion causes a drop in heat transmission as Pr rises, and low heat conductance causes a decrease in the temperature field. An augmentation in Pr results from an increase in fluid viscosity and a decrease in heat conductivity, which slows the temperature profiles. A superior deteriorating trend in the fluid temperature is detected due to the fluid constant thermal conductivity as compared to variable case. The characteristics of temperature in relation to Eckert number are shown in Fig. 5. In nanofluids, the temperature profile that corresponds to the Eckert number rises. Eckert number maximizes fluid temperature since it can produce additional heat in the system. In the situation of fluctuating and constant thermal conductivity, we contrasted the impact of Eckert number. The thermal profile marginally rises as the nanoparticle's constant thermal conductivity parameter. However, by increasing the values of the variable thermal conductivity number from 0 to 0.5, the rate of increase of the temperature profile is significantly bigger. The same thing happens for different Eckert number values, demonstrating that heat is increased by kinetic energy. Physically, it is consistent with the evacuation of energy from fluid regions because of viscosity and elastic deformation. The motion of suspended nanoparticles influences the effectiveness of the thermal conductivity of nanoliquids. There is an interaction between the particles and the channel wall because of the suspension of nanoparticles in the fluid, the contact between the base fluid and solid particles. Fig. 6 illustrates how the Brownian diffusion (or particle-density increment) parameter affects temperature. The thermal layer thickness and surface temperature both increase as the Brownian diffusion parameter value

Table 1

Matched numerical results for velocity field, when $We = 0$, (Newtonian fluid case is revert) $f(\zeta)$, while $Re = 50$.

α	Moradi et al. [60]	Rana et al. [61]	Carreau fluid model
1^0	0.9825	0.9825	0.982613
2^0	0.9316	0.9316	0.931567
3^0	0.8513	0.8513	0.851350
4^0	0.7482	0.7482	0.748219

Table 2
Matched numerical results for velocity field, when $We = 0$, (Newtonian fluid case is revert) $f(\zeta)$ and skin friction $f'(1)$, while $Re = 50$.

ζ	Carreau fluid velocity $f(\zeta)$	Carreau fluid Skin friction $f'(1)$	Mosta et al. [62] velocity $f(\zeta)$	Mosta et al. [62] Skin friction $f'(1)$
0.0	1	-3.5394108	1.000000	-3.539416
0.1	0.9824195	-3.3869190	0.982431	-3.386911
0.2	0.93122698	-2.9577910	0.931226	-2.957792
0.3	0.85061769	-2.3285721	0.850611	-2.328574
0.4	0.74678456	-1.6017891	0.746791	-1.601789
0.5	0.6269449	-0.8797939	0.626948	-0.879794
0.6	0.4982933	-0.2439481	0.498234	-0.243949
0.7	0.3669425	0.2556009	0.366966	0.255607
0.8	0.2381901	0.5997010	0.238124	0.599702
0.9	0.1151834	0.7930090	0.115152	0.793004
1.0	0.0000000	0.8543690	0.000000	0.854369

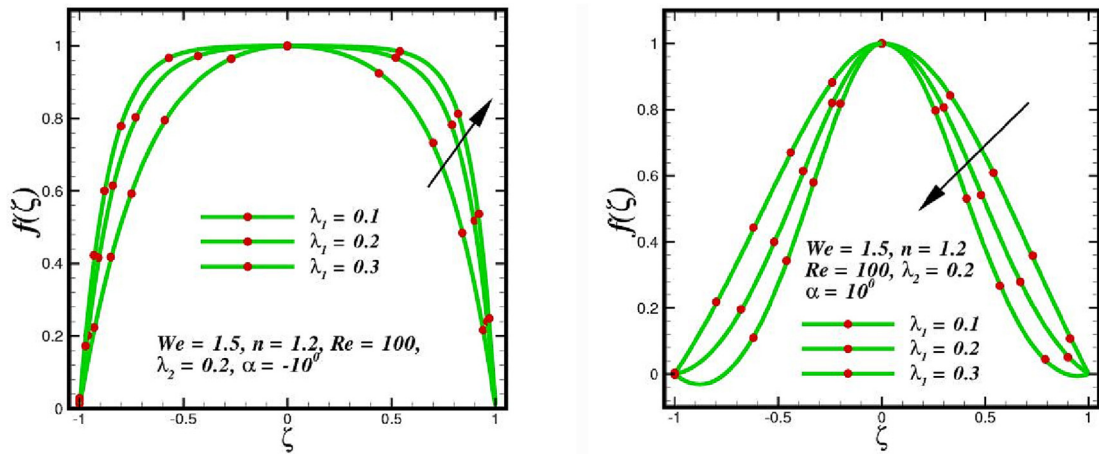


Fig. 2. Flow regime in a channel sections under the influence of λ_1 .

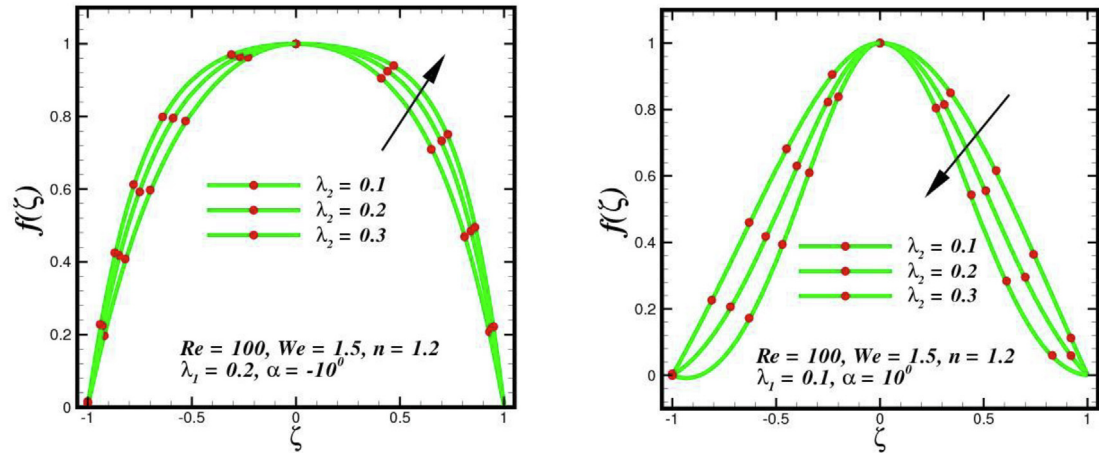


Fig. 3. Flow regime in a channel section under the influence of λ_2 .

increases. The temperature of the nanofluid increases because of this behavior. Fig. 7 illustrates how the temperature is significantly influenced by the adjusted diffusivity ratio parameter (thermophoresis parameter). The variance in the temperature and velocity profiles is shown to be greatly enhanced by enhancing the thermophoresis effect (D_T). That makes sense given that a high value of D_T is linked to a thick thermal boundary layer and a low surface temperature gradient. As a result, improving the thermophoresis parameter value improves the temperature distribution. Moreover, a higher temperature produces more kinetic

energy, which raises the heat transfer rate. The temperature distribution attribute results from the heated fluid within the channel reducing the contact between the fluid molecules, whereas the inner side and outside channel has the reverse effect. In the center of the channel is where the inflection happens, the temperature is significantly higher. Fig. 8 shows how the thermal conductivity parameter ε_1 affects fluid temperature. The temperature rises in the converging and diverging zones as increases. From a physical standpoint, these results show that the thermal conductivity parameter plays a significant part in increasing the magnitude of

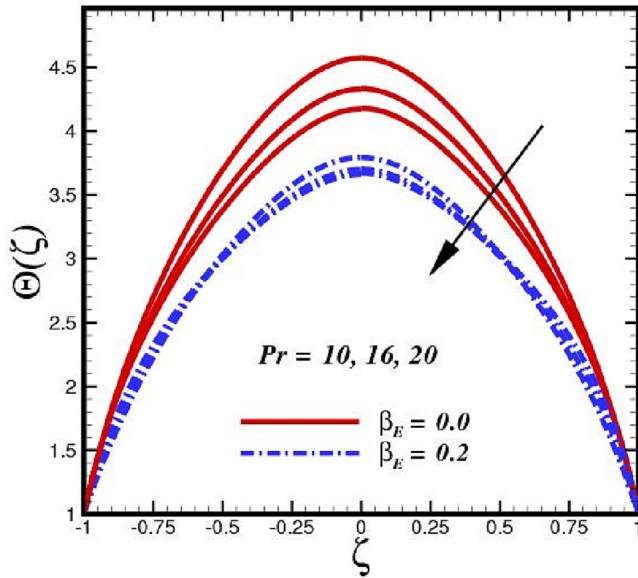


Fig. 4. Temperature sketches due to Pr .

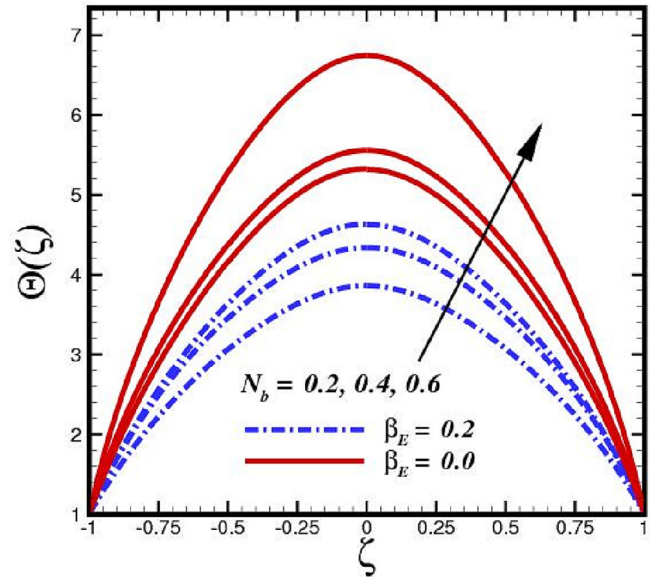


Fig. 6. Temperature sketches due to N_b .

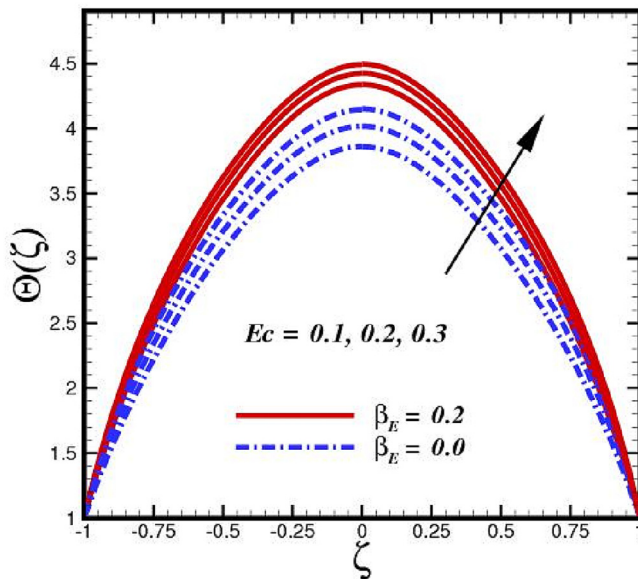


Fig. 5. Temperature sketches due to Ec .

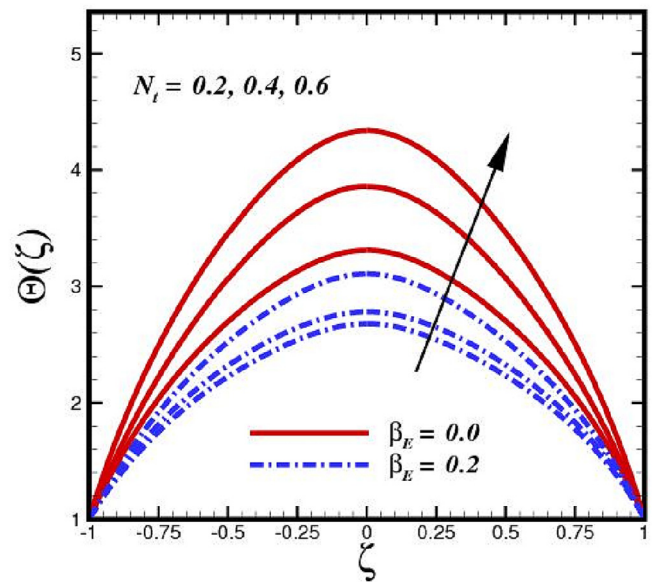


Fig. 7. Temperature sketches due to N_t .

the temperature field. The figure shows that as increases, the effects of thermal conductivity increase with the boundary layer, leading to an increase in temperature field.

4.3. Volumetric concentration analysis

The variation in concentration $\Phi(\zeta)$ under various physical dimensionalities are depicted in Figs. 9–11. The Brownian motion, which is caused by thermal energy, is a phenomenon known as thermal motion. It involves the continual random movement of atoms and molecules in a liquid or gas (Robert Brown, [63]). The Brownian motion may manifest itself in lower viscosity molecules, smaller molecular sizes, and higher temperature. The ratio of heat diffusion in the nanofluid to Brownian motion-induced nanoparticle diffusion is known as the Brownian motion parameter (N_b). The

Brownian motion can be increased by increasing the particle diameter because, based on the Einstein-Stokes equation (Buongiorno, [64]). As a result, the enhanced values of N_b (Fig. 9) diminishes the fluid concentration. The Brownian motion parameter (N_b) has a natural effect on enhancing the diffusion of nanoparticles, which causes the particles to naturally migrate from the channel mainstream to the free stream. As a result, the thermal boundary layer expands. The nanoparticle species, however, exhibit the opposite behavior. Layers of molar species are suppressed and concentrated based on their effects. Maximum fluid temperature is reached at $N_b = 0.8$, which results in more nanoparticle mobility with the layer. The mobility of nanoparticles close to the wall is physically influenced by the temperature gradient created by thermophoretic forces (N_t) between the heated fluid and the non-heated wall (Fig. 10). Therefore, whereas N_t promotes the formation of molar species layers, concentration increases the width of the thermal boundary layer. When microscopic fluid particles are dragged back

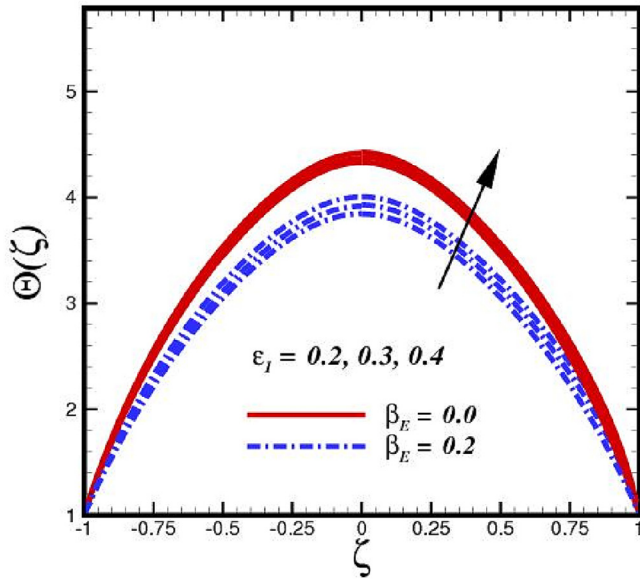


Fig. 8. Temperature sketches due to ε_1 .

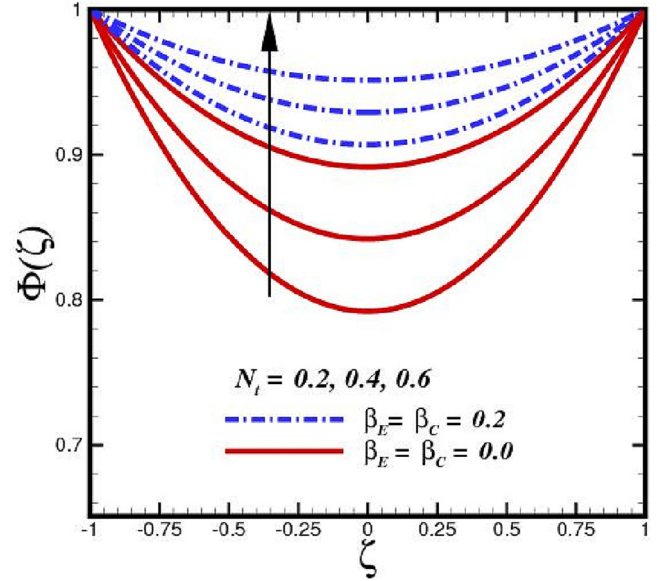


Fig. 10. Mass species sketches due to N_t .

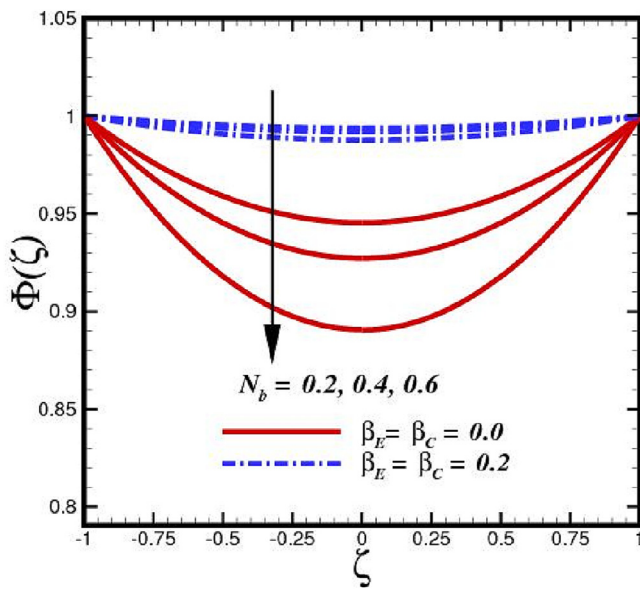


Fig. 9. Mass species sketches due to N_b .

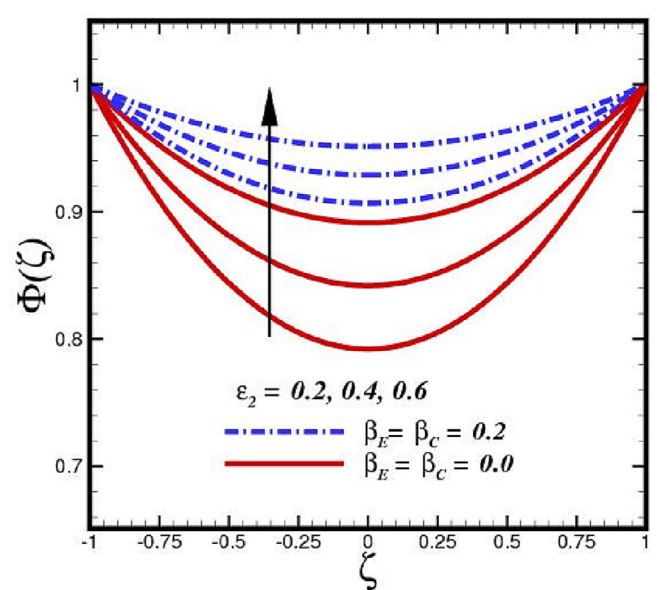


Fig. 11. Mass species sketches due to ε_2 .

from a warm to a cold place, it is termed the thermophoresis process. The nanofluid particles then move away from the heated surface, improving the density profile of the nanoparticles. Fig. 11 illustrates the effect of the mass diffusivity parameter ε_2 on the concentration field. The concentration rises in both the divergent and convergent zones as ε_2 increases. Physically, these results show that the mass diffusivity parameter is a key factor in increasing the amplitude of the concentration field. According to the figure, as ε_2 is increased, mass diffusivity effects become stronger with the boundary layer, leading to an increase in concentration field.

4.4. Entropy and Bejan analysis

Entropy generation simply refers to the amount of entropy needed for irreversible processes. By increasing N_t , the thermophoretic force continues to produce entropy far from the chan-

nel walls (Fig. 12). The viscous effect is greater than the heat transfer influence closer to the channel wall by enhancing the impact of thermophoretic diffusion. It enables in declining Be . However, away from the centre, the growing thermophoretic diffusion is dominated by the heat transport impact, which overcomes the viscous effect, leading to an improvement in E_C . According to Fig. 13, higher N_b reduces entropy production E_C close to the channel centre, whereas it increases far away from the wall. The same characteristic of the Bejan number Be towards N_b is clearly seen in Fig. 13. The increase in N_b encourages nanoparticle Brownian motion. As a result, heat is transmitted to the farthest location and nanoparticles kinetic energy is enriched. Thus, entropy generation takes place far from the walls. When N_b is raised in the vicinity of the walls, the viscous effect becomes more intense compared to the irreversibility of heat transfer, creating resistance in Be . After a predetermined distance, the heat transfer becomes strengthened for expanding N_b , which causes an increase in Be .

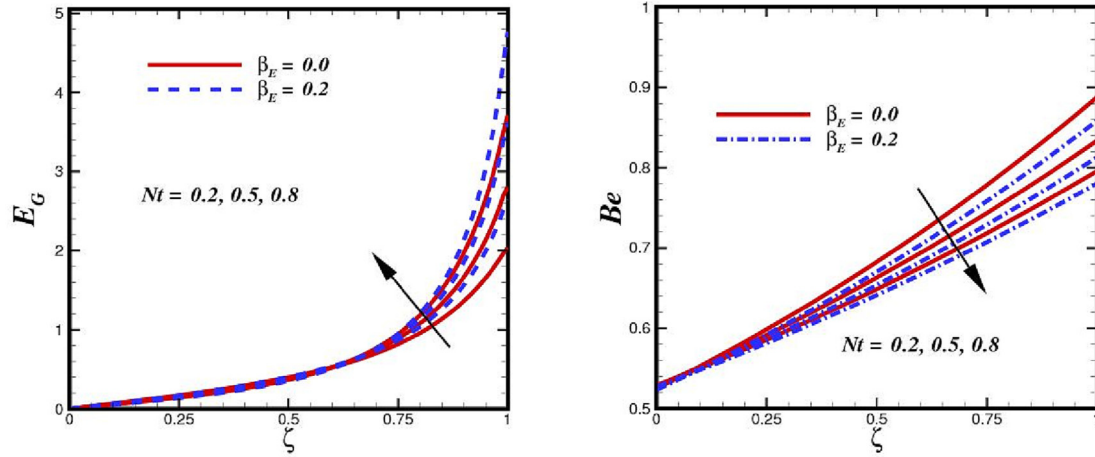


Fig. 12. Comparison (with and without thermal relaxation time) of entropy generation rate and Bejan profile due to variation of N_t .

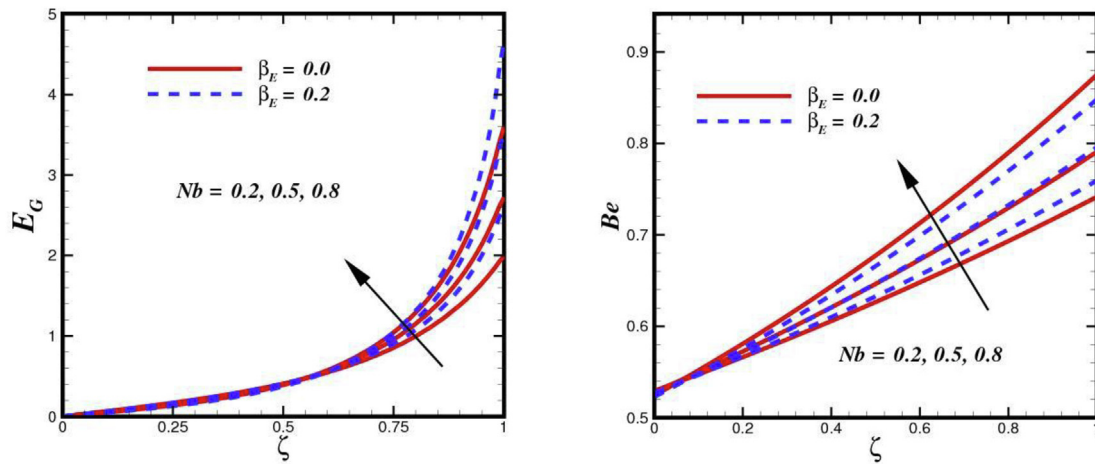


Fig. 13. Comparison (with and without thermal relaxation time) of entropy generation rate and Bejan profile due to variation of N_b .

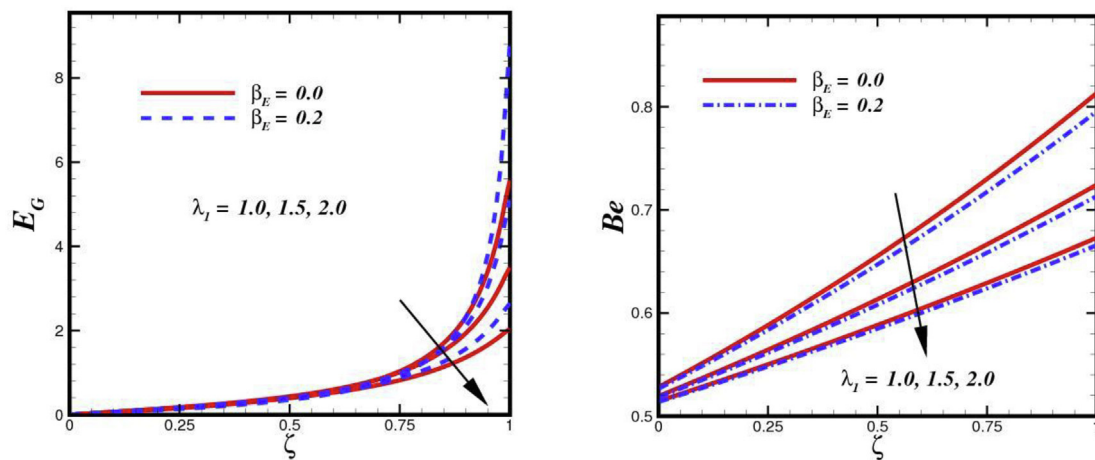


Fig. 14. Comparison (with and without thermal relaxation time) of entropy generation rate and Bejan profile due to variation of λ_1 .

Fig. 14 shows how the porosity parameter affects E_G and Be for various layouts under geometrical angle of inclination α . Because porous media have a low permeability and a high liquid-movement resistance, the nanoliquid cannot freely permeate the porous media. Conduction mode of heat transfer used in this instance.

Be plot can also be used to support this. The Bejan value for lower λ_1 is greater than 0.5, indicating that only conduction mode may occur when heat transfer entropy is dominating. As λ_1 increases, the permeability improves and the resistance to liquid flow decreases, which triggers convection. With further improvement

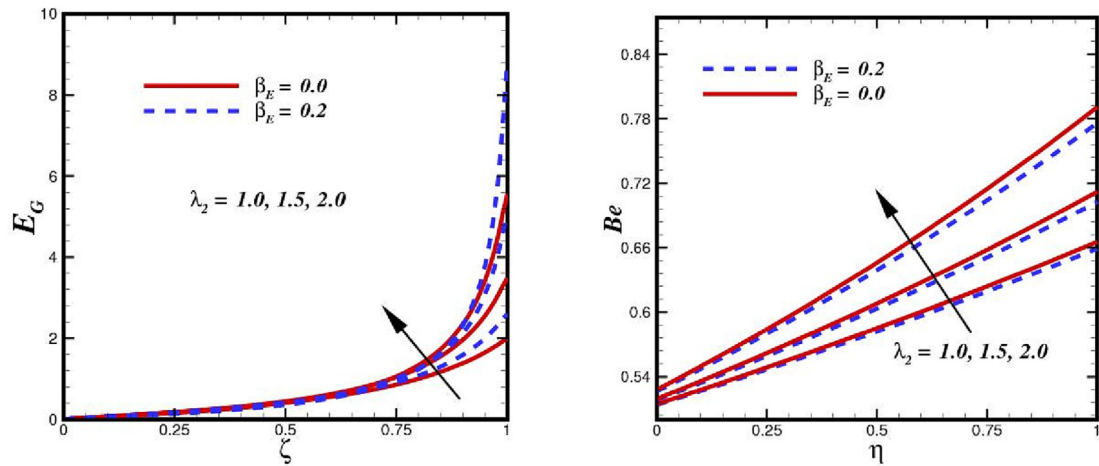


Fig. 15. Comparison (with and without thermal relaxation time) of entropy generation rate and Bejan profile due to variation of λ_2 .

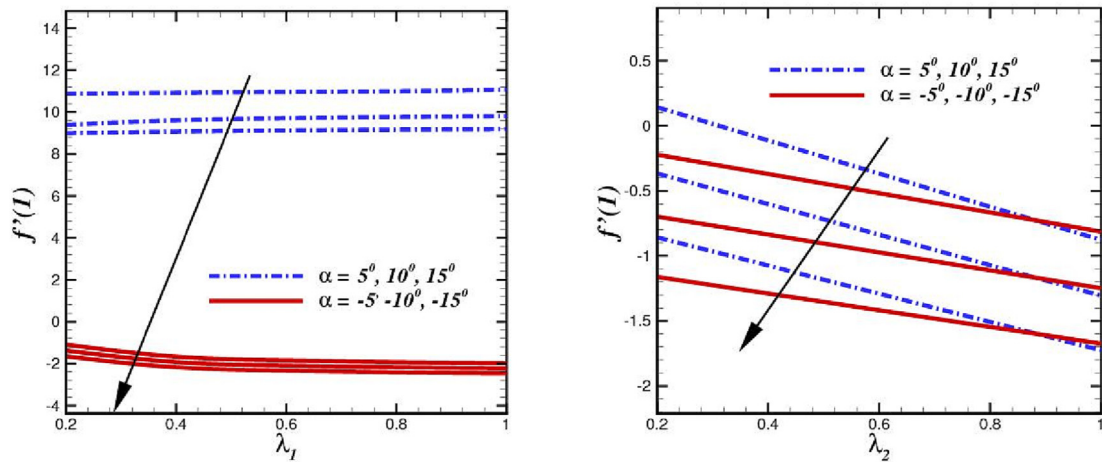


Fig. 16. Comparative analysis of skin friction within converging and divergent channel against λ_1 and λ_2 .

in λ_1 , the porous medium permeability improves and makes it easier for liquid to pass through. This increases friction irreversibility, improves E_C , and exhibits noticeable variety in improving λ_1 . The strength of the flow will be larger in a non-porous container because the liquid does not encounter porous drag. This causes

more friction entropy to be produced, which improves E_C . Due to the high viscosity, the flow strength declines, which results in reduced friction entropy formation and lowers λ_1 . The Bejan number is increasing, as seen in the figure, which indicates that fluid friction entropy is reducing. Fig. 15 highlight the key characteris-

Table 3
Numerical computations representing temperature against various parameter in a convergent channel when, $\alpha = -10^\circ$.

Pr	We	n	N_b	N_t	Ec	$\Theta(\zeta)\beta_E = 0.0$	$\Theta(\zeta)\beta_E = 0.5$
7	1.0	1.2	0.4	0.2	0.1	1.1338	1.2696
10						1.1617	1.3851
13						1.1802	1.5006
7	1.0	1.2	0.4	0.2	0.1	1.1350	1.2961
	1.2					1.1372	1.2696
	1.4					1.1392	1.2743
7	1.0	1.2	0.4	0.2	0.1	1.1328	1.2790
		1.4				1.1432	2.1687
		1.6				1.1564	2.2880
7	1.0	1.2	0.4	0.2	0.1	1.1326	2.0783
			0.6			1.1328	2.0784
			0.8			1.1330	2.0785
7	1.0	1.2	0.4	0.2	0.1	1.1328	1.2694
				0.4		1.1261	1.2693
				0.6		1.1230	1.2692
7	1.0	1.2	0.4	0.2	0.1	1.1934	1.2696
					0.2	1.2210	1.5391
					0.3	1.2271	1.8087

Table 4Numerical computations representing temperature distribution against various parameter in a diverging channel when, $\alpha = 10^0$.

Pr	We	n	N_b	N_t	Ec	$\Theta(\zeta)\beta_E = 0.0$	$\Theta(\zeta)\beta_E = 0.5$
7	1.0	1.2	0.4	0.2	0.1	1.1468	1.2961
10						1.1602	1.4230
13						1.1723	1.5498
7	1.0	1.2	0.4	0.2	0.1	1.1368	1.2994
						1.1371	1.3029
						1.1374	1.3064
7	1.0	1.2	0.4	0.2	0.1	1.1368	1.2961
		1.4				1.1393	1.3116
		1.6				1.1439	1.3333
7	1.0	1.2	0.4	0.2	0.1	1.1368	1.2961
			0.6			1.1371	1.2959
			0.8			1.1378	1.2961
7	1.0	1.2	0.4	0.2	0.1	1.1368	1.2961
				0.4		1.1311	1.2960
				0.6		1.1260	1.2955
7	1.0	1.2	0.4	0.2	0.1	1.1368	1.5921
					0.2	1.1828	1.8882
					0.3	1.1900	2.1843

tics of the Darcy parameter (λ_2) on E_G and Be . In fact, when the value of (λ_2) rises, there is an increase in the amount of resistance created by friction and interactions between nanoparticles, which increases kinetic energy. For both convergent and divergent channels, E_G and Be are therefore enhanced.

Fig. 16 shows the impact of the porosity parameter λ_1 and Forchheimer number λ_2 on the frictional drag factor C_f of Carreau nanofluid. The plot of the drag coefficient decreases as the Carreau nanofluid increases, and the related boundary layer thickens as well. Additionally, it was found that for higher valuations of λ_1 and λ_2 , the friction factor decreases.

The comparison of temperature distribution within converging channel and diverging channel in the existence of non-Fourier heat and Fourier's heat flux theory are presented through Table 3 and Table 4, respectively. The computational outcomes reveals that the augmentation of temperature field with growing Prandtl Pr , Brownian motion parameter N_b , and Eckert number Ec , Wiesen-berg number We can be seen. Temperature profiles around the central area of the channel tend to climb as N_b upturns. According to the description of Brownian motion, rising Nb results from the sparseness of the fluid viscosity. Consequently, the kinetic energy of the nanoparticles is increased by the irregular flow movement, which advances the temperature of the nanofluid. Moreover, the nature of the thermophoresis parameter causes the flow field viscosity to decrease and the temperature distribution to increase.

The results reveal that the thermal relaxation time parameter weakens the temperature profiles of the Carreau nanofluids. Furthermore, the temperature growth within diverging wedge is substantially higher as compared to convergent channel. In the likewise scenario Table 5 and Table 6 are depicted to assess the volumetric concentration of the nanoparticles in the presence of Fickian's parameter β_C . A reverse trend for concentration is observed in the presence of Fickian's parameter β_C is perceived. Concentration distribution against various parameters is found higher in case of Fick's law.

5. Conclusion

The comparative analysis of entropy optimization and irreversibility (Bejan number) for the flow of an incompressible non-Newtonian nanofluid through a non-intersecting channel wall using Darcy-Forchheimer model is investigated. The non-Fourier's and Fickian's models are utilized to explore the phenomena of heat and mass transfer. Buongiorno's framework has been taken into consideration for investigating the effects of Brownian and thermophoresis migration over fluid flow. The physical problem is modeled in the shape of three non-linear partial differential equations. The modeled equations are transformed and solved using Bvp4c technique strategy with the shooting method. The current approximations solutions are adjudged in limiting cases

Table 5Numerical computations representing temperature distribution against various parameter in a convergent channel when, $\alpha = -10^0$.

Pr	We	n	N_b	N_t	Ec	$\Phi(\zeta)\beta_E = \beta_C = 0.0$	$\Phi(\zeta)\beta_E = \beta_C = 0.5$
7	1.0	1.2	0.4	0.2	0.1	0.1271	0.2158
10						0.1502	0.2230
13						0.1743	0.2310
7	1.0	1.2	0.4	0.2	0.1	0.1902	0.2024
						0.1973	0.3019
						0.1990	0.3039
7	1.0	1.2	0.4	0.2	0.1	0.1268	0.2269
		1.4				0.1395	0.2316
		1.6				0.1449	0.3345
7	1.0	1.2	0.4	0.2	0.1	0.1349	0.2161
			0.6			0.1314	0.2011
			0.8			0.1289	0.1923
7	1.0	1.2	0.4	0.2	0.1	0.1369	0.2159
				0.4		0.1489	0.2260
				0.6		0.1560	0.2339
7	1.0	1.2	0.4	0.2	0.1	0.1368	0.1998
					0.2	0.1389	0.2082
					0.3	0.1400	0.2143

Table 6Numerical computations representing temperature distribution against various parameter in a convergent channel when, $\alpha = 10^0$.

Pr	We	n	N_b	N_t	Ec	$\Phi(\zeta)\beta_E = \beta_C = 0.0$	$\Phi(\zeta)\beta_E = \beta_C = 0.5$
7	1.0	1.2	0.4	0.2	0.1	0.1329	0.2439
10						0.1498	0.2508
13						0.1530	0.2629
7	1.0	1.2	0.4	0.2	0.1	0.1329	0.2125
						0.1460	0.2329
						0.1569	0.2498
7	1.0	1.2	0.4	0.2	0.1	0.1328	0.2408
		1.4				0.1492	0.2590
		1.6				0.1549	0.2648
7	1.0	1.2	0.4	0.2	0.1	0.1568	0.2389
			0.6			0.1498	0.2289
			0.8			0.1370	0.2103
7	1.0	1.2	0.4	0.2	0.1	0.1368	0.2440
						0.1412	0.2567
						0.1598	0.2649
7	1.0	1.2	0.4	0.2	0.1	0.1369	0.2409
					0.2	0.1579	0.2611
					0.3	0.1720	0.2810

such as viscous case. The key outcomes associated with the current quest are outlined here:

1. The Carreau fluid velocity escalates for higher estimation of inertia parameter λ_2 and porosity parameter λ_1 in convergent channel, while opposite trend is noticed in divergent channel.
2. Entropy and Bejan optimize against inertia parameter λ_2 and dwindle with porosity factor λ_1 .
3. Strengthening the temperature field is possible due to the thermophoresis mechanism and Brownian motion of nanoparticles.
4. The temperature augmented with Eckert number Ec , heat source λ . However, the nanofluid thermal performance deteriorated with Prandtl number Pr .
5. The thermal performance of fluid can be amplified with variable thermal conductivity ϵ_1 .
6. The heat and mass transfer rate are higher and with the presence of variables thermal conductivity parameter ϵ_1 and mass diffusivity ϵ_2 .
7. Skin friction is decreasing function of λ_1 and λ_2 .
8. The Cattaneo Christov heat flux model is attained by implementing the thermal relaxation parameter, and it is discovered that using the model for both convergent and diverging channels causes the fluid temperature to drop.

CRediT authorship contribution statement

Nidhal Ben Kheder: Data curation, Writing – review & editing. **Sohail Rehman:** Conceptualization, Writing – original draft. **Sultan Alqahtani:** Software, Writing – review & editing. **Hashim:** Methodology, Validation. **Sultan Alshehry:** Formal analysis, Writing – review & editing.

Declaration of Competing Interest

The authors declare that they have no known competing financial interests or personal relationships that could have appeared to influence the work reported in this paper.

Acknowledgment:

The authors extend their appreciation to the Deanship of Scientific Research at King Khalid University for funding this work through large group Research Project under grant number RGP2/290/44.

References

- [1] J.B.J. Fourier, *Théorie analytique de la chaleur*, F. Didot, Paris, 1822.
- [2] C. c., Sulla Conduzione del Calore, *Atti Sem. Mat. Fis. Univ. Modena* 3 (1948) 83–101.
- [3] V. Tibullo, V. Zampoli, A uniqueness result for the Cattaneo-Christov heat conduction model applied to incompressible fluids, *Mech. Res. Commun.* 38 (2011) 77–79, <https://doi.org/10.1016/j.mechrescom.2010.10.008>.
- [4] B. Straughan, Thermal convection with the Cattaneo-Christov model, *Int. J. Heat Mass Transf.* 53 (2010) 95–98, <https://doi.org/10.1016/j.ijheatmasstransfer.2009.10.001>.
- [5] S.A.M. Haddad, Thermal instability in Brinkman porous media with Cattaneo-Christov heat flux, *Int. J. Heat Mass Transf.* 68 (2014) 659–668, <https://doi.org/10.1016/j.ijheatmasstransfer.2013.09.039>.
- [6] T. Hayat, F. Shah, A. Alseadi, Cattaneo-Christov double diffusions and entropy generation in MHD second grade nanofluid flow by a Riga wall, *Int. Commun. Heat Mass Transfer* 119 (2020), <https://doi.org/10.1016/j.icheatmasstransfer.2020.104824>.
- [7] M.E. Ali, N. Sandeep, Cattaneo-Christov model for radiative heat transfer of magnetohydrodynamic Casson-ferrofluid: a numerical study, *Results Phys.* 7 (2017) 21–30, <https://doi.org/10.1016/j.rinp.2016.11.055>.
- [8] H. Waqas, M. Fida, D. Liu, U. Manzoor, T. Muhammad, Numerical simulation of entropy generation for nanofluid with the consequences of thermal radiation and Cattaneo-Christov heat flux model, *Int. Commun. Heat Mass Transfer* 137 (2022), <https://doi.org/10.1016/j.icheatmasstransfer.2022.106293>.
- [9] G. Kumaran, R. Sivaraj, V. Ramachandra Prasad, O. Anwar Beg, H.-H. Leung, F. Kamalov, Numerical study of axisymmetric magneto-gyrotactic bioconvection in non-Fourier tangent hyperbolic nano-functional reactive coating flow of a cylindrical body in porous media, *Eur. Phys. J. Plus.* 136 (2021) 1107, <https://doi.org/10.1140/epjp/s13360-021-02099-z>.
- [10] R. Ghosh, T.M. Agbaje, S. Mondal, S. Shaw, Bio-convective viscoelastic Casson nanofluid flow over a stretching sheet in the presence of induced magnetic field with Cattaneo-Christov double diffusion, *Int. J. Biomath.* 15 (2022) 2150099, <https://doi.org/10.1142/S1793524521500996>.
- [11] A. Bejan, Second law analysis in heat transfer, *Energy* 5 (1980) 720–732, [https://doi.org/10.1016/0360-5442\(80\)90091-2](https://doi.org/10.1016/0360-5442(80)90091-2).
- [12] A. Bejan, Entropy generation minimization: The new thermodynamics of finite-size devices and finite-time processes, *J. Appl. Phys.* 79 (1996) 1191–1218, <https://doi.org/10.1063/1.362674>.
- [13] A. Mahesh, S.V.K. Varma, C.S.K. Raju, M.J. Babu, K. Vajravelu, W. Al-Kouz, Significance of non-Fourier heat flux and radiation on PEG – Water based hybrid Nanofluid flow among revolving disks with chemical reaction and entropy generation optimization, *Int. Commun. Heat Mass Transfer* 127 (2021), <https://doi.org/10.1016/j.icheatmasstransfer.2021.105572>.
- [14] P.S. Reddy, P. Sreedevi, V.N. Reddy, Entropy generation and heat transfer analysis of magnetic nanofluid flow inside a square cavity filled with carbon nanotubes, *Chemical Thermodynamics and Thermal Analysis* 6 (2022), <https://doi.org/10.1016/j.ctta.2022.100045>.
- [15] P. Mondal, T.R. Mahapatra, MHD double-diffusive mixed convection and entropy generation of nanofluid in a trapezoidal cavity, *Int. J. Mech. Sci.* 208 (2021), <https://doi.org/10.1016/j.ijmecsci.2021.106665>.
- [16] T. Hayat, K. Muhammad, S. Momani, Numerical study of entropy generation in Darcy-Forchheimer (D-F) Bödewadt flow of CNTs, *Int. J. Hydrogen Energy* 46 (2021) 34449–34462, <https://doi.org/10.1016/j.ijhydene.2021.08.013>.
- [17] N.N. Kumar, D.R.V.S.R.K. Sastry, S. Shaw, Irreversibility analysis of an unsteady micropolar CNT-blood nanofluid flow through a squeezing channel with activation energy-Application in drug delivery, *Comput. Methods Programs Biomed.* 226 (2022), <https://doi.org/10.1016/j.cmpb.2022.107156>.

- [18] S. Mandal, G.C. Shit, S. Shaw, O.D. Makinde, Entropy analysis of thermo-solutal stratification of nanofluid flow containing gyrotactic microorganisms over an inclined radiative stretching cylinder, *Thermal Sci. Eng. Prog.* 34 (2022), <https://doi.org/10.1016/j.tsep.2022.101379> 101379.
- [19] M.I. Khan, T.A. Khan, S. Qayyum, T. Hayat, M.I. Khan, A. Alsaedi, Entropy generation optimization and activation energy in nonlinear mixed convection flow of a tangent hyperbolic nanofluid, *Eur. Phys. J. Plus.* 133 (2018) 329, <https://doi.org/10.1140/epjp/i2018-12093-y>.
- [20] M. Ijaz Khan, S. Ullah, T. Hayat, M. Waqas, M. Imran Khan, A. Alsaedi, Salient aspects of entropy generation optimization in mixed convection nanomaterial flow, *Int. J. Heat Mass Transf.* 126 (2018) 1337–1346, <https://doi.org/10.1016/j.ijheatmasstransfer.2018.05.168>.
- [21] M.M. Bhatti, O.A. Bég, R. Ellahi, T. Abbas, Natural convection non-Newtonian EMHD dissipative flow through a microchannel containing a non-Darcy porous medium: Homotopy perturbation method study, *Qual. Theory Dyn. Syst.* 21 (2022) 97, <https://doi.org/10.1007/s12346-022-00625-7>.
- [22] L.E. Sorokin, Stability of flow with the thermal conductivity depending linearly on the temperature, *Fluid Dyn.* 32 (1997) 309–312.
- [23] A. Pinarbasi, C. Ozalp, S. Duman, Influence of variable thermal conductivity and viscosity for nonisothermal fluid flow, *Phys. Fluids* 17 (3) (2005) 038109.
- [24] M. Khan, T. Salahuddin, E.-S.-M. Sherif, H.S. Abdo, Wall slip characteristics on the dynamics of radiative Carreau fluid flow subjected to thermophysical properties of the rotating boundary layer, *Int. Commun. Heat Mass Transfer* 119 (2020), <https://doi.org/10.1016/j.icheatmasstransfer.2020.104960> 104960.
- [25] M. Sohail, U. Nazir, Y.-M. Chu, H. Alrabaiiah, W. Al-Kouz, P. Thounthong, Computational exploration for radiative flow of Sutterby nanofluid with variable temperature-dependent thermal conductivity and diffusion coefficient, *Open. Physics* 18 (2020) 1073–1083, <https://doi.org/10.1515/phys-2020-0216>.
- [26] T. Naseem, U. Nazir, E.R. El-Zahar, A.M. Algelany, M. Sohail, Numerical computation of Dufour and Soret effects on radiated material on a porous stretching surface with temperature-dependent thermal conductivity, *Fluids* 6 (2021) 196, <https://doi.org/10.3390/fluids6060196>.
- [27] N. Tarakaramu, P.V.S. Narayana, B. Venkateswarlu, Numerical simulation of variable thermal conductivity on 3D flow of nanofluid over a stretching sheet, *Nonlinear. Engineering* 9 (2020) 233–243, <https://doi.org/10.1515/nleng-2020-0011>.
- [28] A.O. Ajibade, A.M. Umar, Mixed convection flow in a vertical channel in the presence of wall conduction, variable thermal conductivity and viscosity, *Nonlinear. Engineering* 9 (2020) 412–431, <https://doi.org/10.1515/nleng-2020-0026>.
- [29] M.F. Ahmed, A. Zaib, F. Ali, O.T. Bafakeeh, E.S.M. Tag-ElDin, K. Guedri, S. Elattar, M.I. Khan, Numerical computation for gyrotactic microorganisms in MHD radiative Eyring-Powell nanomaterial flow by a static/moving wedge with Darcy-Forchheimer relation, *Micromachines* 13 (2022) 1768, <https://doi.org/10.3390/mi13101768>.
- [30] M.M. Bhatti, H.F. Öztop, R. Ellahi, Study of the magnetized hybrid nanofluid flow through a flat elastic surface with applications in solar energy, *Materials* 15 (2022) 7507, <https://doi.org/10.3390/ma15217507>.
- [31] F. Rehman, M.I. Khan, M. Sadiq, A. Malook, MHD flow of carbon in micropolar nanofluid with convective heat transfer in the rotating frame, *J. Mol. Liq.* 231 (2017) 353–363, <https://doi.org/10.1016/j.molliq.2017.02.022>.
- [32] G.B. Jeffery, L. The two-dimensional steady motion of a viscous fluid, *The London, Edinburgh, and Dublin Philosophical Magazine and Journal of Science.* 29 (1915) 455–465. doi: 10.1080/14786440408635327.
- [33] G. Hamel, *Spiralförmige Bewegungen zäher Flüssigkeiten, Jahresber. Deutsch. Math.-Verein.* 25 (1917) 34–60.
- [34] L. Rosenhead, G.I. Taylor, The steady two-dimensional radial flow of viscous fluid between two inclined plane walls, *Proceedings of the Royal Society of London. Series A. Mathematical and Physical Sciences.* 175 (1940) 436–467. doi: 10.1098/rspa.1940.0068.
- [35] K. Millsaps, K. Pohlhausen, Thermal distributions in Jeffery-Hamel flows between nonparallel plane walls, *J. Aeronautical Sci.* 20 (1953) 187–196, <https://doi.org/10.2514/8.2587>.
- [36] R.I. Tanner, Non-Newtonian fluid parameter estimation using conical flows, *Ind. Eng. Chem. Fund.* 5 (1966) 55–59, <https://doi.org/10.1021/i160017a009>.
- [37] A. Hooper, B.R. Duffy, H.K. Moffatt, Flow of fluid of non-uniform viscosity in converging and diverging channels, *J. Fluid Mech.* 117 (1982) 283–304, <https://doi.org/10.1017/S0022112082001633>.
- [38] A.M. Hull, J.R.A. Pearson, On the converging flow of viscoelastic fluids through cones and wedges, *J. Nonnewton. Fluid Mech.* 14 (1984) 219–247, [https://doi.org/10.1016/0377-0257\(84\)80046-4](https://doi.org/10.1016/0377-0257(84)80046-4).
- [39] S. Rehman, Hashim, Y. Trabelsi, S. Alqahtani, S. Alshehry, S.M. Eldin, A renovated Jeffery-Hamel flow problem and new scaling statistics for heat, mass fluxes with Cattaneo-Christov heat flux model, *Case Stud. Thermal Eng.* 43 (2023) 102787.
- [40] M. Boujelbene, S. Rehman, Hashim, S. Alqahtani, S.M. Eldin, Optimizing thermal characteristics and entropy degradation with the role of nanofluid flow configuration through an inclined channel, *Alex. Eng. J.* 69 (2023) 85–107.
- [41] M. Boujelbene, S. Rehman, S. Alqahtani, S. Alshehry, S.M. Eldin, Thermal transport and magnetohydrodynamics flow of generalized Newtonian nanofluid with inherent irreversibility between conduit with slip at the walls, *Eng. Appl. Comput. Fluid Mech.* 17 (2023) 2182364, <https://doi.org/10.1080/19942060.2023.2182364>.
- [42] P.J. Carreau, Rheological equations from molecular network theories, *Trans. Soc. Rheol.* 16 (1972) 99–127, <https://doi.org/10.1122/1.549276>.
- [43] M. Khan, M. Azam, A. Munir, On unsteady Falkner-Skan flow of MHD Carreau nanofluid past a static/moving wedge with convective surface condition, *J. Mol. Liq.* 230 (2017) 48–58, <https://doi.org/10.1016/j.molliq.2016.12.097>.
- [44] T. Hayat, A. Aziz, T. Muhammad, A. Alsaedi, An optimal analysis for Darcy-Forchheimer 3D flow of Carreau nanofluid with convectively heated surface, *Results Phys.* 9 (2018) 598–608, <https://doi.org/10.1016/j.rinp.2018.03.009>.
- [45] M. Ijaz Khan, M. Nigar, T. Hayat, A. Alsaedi, On the numerical simulation of stagnation point flow of non-Newtonian fluid (Carreau fluid) with Cattaneo-Christov heat flux, *Comput. Methods Programs Biomed.* 187 (2020), <https://doi.org/10.1016/j.cmpb.2019.105221> 105221.
- [46] S. Edwards, Dynamics of polymeric liquids vol. 1, fluid mechanics, edited by R. B. Bird, R. C. Armstrong and O. Hassager, Wiley Interscience, New York, 1987, pp. xxi + 649, price £64.15. ISBN 0-471-80245-X. Vol. 2, Kinetic theory, edited by R. B. Bird, C. F. Curtiss, R. C. Armstrong and O. Hassager, Wiley-Interscience, New York, 1987. pp. xxi + 437, price 659.65. ISBN 0-471-80244-1, British Polymer Journal. 20 (1988) 299–299. doi: 10.1002/pi.4980200323.
- [47] D.V. Boger, Demonstration of upper and lower Newtonian fluid behaviour in a pseudoplastic fluid, *Nature* 265 (1977) 126–128, <https://doi.org/10.1038/265126a0>.
- [48] S. Ahmad, M. Farooq, Double-diffusive Hamel-Jeffrey flow of nanofluid in a convergent/divergent permeable medium under zero mass flux, *Sci Rep.* 13 (2023) 1102, <https://doi.org/10.1038/s41598-023-27938-0>.
- [49] S. Ahmad, S. Sheriff, A. Anjum, M. Farooq, Analysis of hydromagnetically modulated multiple slips motion of hybrid-nanofluid through a converging/diverging moving channel, *Proceedings of the Institution of Mechanical Engineers, Part E: Journal of Process Mechanical Engineering.* 236 (4) (2022) 1377–1391.
- [50] D. Ramaiah K., S. P., G. Kotha, K. Thangavelu, MHD rotating flow of a Maxwell fluid with Arrhenius activation energy and non-Fourier heat flux model, *Heat Transfer.* 49 (4) (2020) 2209–2227.
- [51] A. Alsaedi, S.A. Khan, T. Hayat, Cattaneo-Christov double diffusive and model development for entropy optimized flow of Reiner-Rivlin material in thermal system and environmental effect, *Alex. Eng. J.* 72 (2023) 67–82, <https://doi.org/10.1016/j.aej.2023.03.079>.
- [52] G. Kumaran, R. Sivaraj, V.R. Prasad, O.A. Beg, R.P. Sharma, Finite difference computation of free magneto-convective Powell-Eyring nanofluid flow over a permeable cylinder with variable thermal conductivity, *Phys. Scr.* 96 (2) (2021) 025222.
- [53] S. Noreen, Qurat Ul Ain, Entropy generation analysis on electroosmotic flow in non-Darcy porous medium via peristaltic pumping, *J. Therm Anal Calorim.* 137 (2019) 1991–2006. doi: 10.1007/s10973-019-08111-0.
- [54] S. Li, M.I. Khan, F. Alzahrani, S.M. Eldin, Heat and mass transport analysis in radiative time dependent flow in the presence of Ohmic heating and chemical reaction, viscous dissipation: an entropy modeling, *Case Stud. Thermal Eng.* 42 (2023), <https://doi.org/10.1016/j.csite.2023.102722> 102722.
- [55] H.T. Basha, R. Sivaraj, Entropy generation of peristaltic Eyring-Powell nanofluid flow in a vertical divergent channel for biomedical applications, *Proceedings of the Institution of Mechanical Engineers, Part E: Journal of Process Mechanical Engineering.* 235 (5) (2021) 1575–1586.
- [56] U. Khan, N. Ahmed, S. Tauseef Mohyud-Din, Thermo-diffusion, diffusion-thermo and chemical reaction effects on MHD flow of viscous fluid in divergent and convergent channels, *Chem. Eng. Sci.* 141 (2016) 17–27.
- [57] A.-S.-J.-A. Al-Saif, A.M. Jasim, New analytical study of the effects thermo-diffusion, diffusion-thermo and chemical reaction of viscous fluid on magneto hydrodynamics flow in divergent and convergent channels, *Appl. Math.* 10 (2019) 268–300, <https://doi.org/10.4236/am.2019.104020>.
- [58] S. Rehman, Hashim, S.I. Ali Shah, Numerical simulation for heat and mass transport of non-Newtonian Carreau rheological nanofluids through convergent/divergent channels, *Proceedings of the Institution of Mechanical Engineers, Part C: Journal of Mechanical Engineering Science.* (2022) 09544062211065688. doi: 10.1177/09544062211065688.
- [59] T. Salahuddin, A. Javed, M. Khan, M. Awais, H. Bangali, The impact of Soret and Dufour on permeable flow analysis of Carreau fluid near thermally radiated cylinder, *Int. Commun. Heat Mass Transfer* 138 (2022), <https://doi.org/10.1016/j.icheatmasstransfer.2022.106378> 106378.
- [60] A. Moradi, A. Alsaedi, T. Hayat, Investigation of nanoparticles effect on the Jeffery-Hamel flow, *Arab J Sci Eng.* 38 (2013) 2845–2853, <https://doi.org/10.1007/s13369-012-0472-2>.
- [61] P. Rana, N. Shukla, Y. Gupta, I. Pop, Homotopy analysis method for predicting multiple solutions in the channel flow with stability analysis, *Commun. Nonlinear Sci. Numer. Simul.* 66 (2019) 183–193, <https://doi.org/10.1016/j.cnsns.2018.06.012>.
- [62] S.S. Motsa, P. Sibanda, F.G. Awad, S. Shateyi, A new spectral-homotopy analysis method for the MHD Jeffery-Hamel problem, *Comput. Fluids* 39 (2010) 1219–1225, <https://doi.org/10.1016/j.compfluid.2010.03.004>.
- [63] R. Brown, XXVII. A brief account of microscopical observations made in the months of June, July and August 1827, on the particles contained in the pollen of plants; and on the general existence of active molecules in organic and inorganic bodies, *The Philosophical Magazine.* 4 (1828) 161–173. doi: 10.1080/14786442808674769.
- [64] J. Buongiorno, Convective transport in nanofluids, *J. Heat Transfer* 128 (2005) 240–250, <https://doi.org/10.1115/1.2150834>.